

REVIEWS OF TOPICAL PROBLEMS

PACS numbers: 72.15.Jf, 72.20.Pa, 85.35.Be

Thermopower in HgTe-based topological insulators and two-dimensional semimetals

G.M. Gusev, Z.D. Kvon, A.D. Levin, E.B. Olshanetsky, N.N. Mikhailov

DOI: https://doi.org/10.3367/UFNe.2025.04.039898

Contents

Abstract. In recent years, there has been a significant effort to investigate the impact of nontrivial electronic topology on the thermoelectric properties of materials. Topological insulators (TIs) and two-dimensional semimetals, in particular, have emerged as an efficient class of thermoelectric materials. When the Fermi level lies within the insulating gap, thermoelectric transport in two-dimensional (2D) topological insulators is primarily determined by the one-dimensional helical states, while in three-dimensional TIs, the transport is driven by the 2D states that exist on the material's surfaces. Here, we review existing results on HgTe quantum wells, which are exemplary in combining the optimal features of topological insulators and the best-performing thermoelectric materials. In addition, we also cover thermoelectric phenomena in two-dimensional semimetals. These materials have overlapping electron and hole bands in the energy space, resulting in a strong mutual friction between them that affects thermoelectric transport and leads to temperature-dependent resistivity. Our review focuses on the thermopower phenomena observed in HgTe-based semimetals, taking into account diffusive and phonon drag effects. Furthermore, we also discuss Weyl two-dimensional semimetals with gapless cone spectra and their thermoelectric properties. We highlight the impact of the coexistence of Dirac and heavy holes in the valence band on the thermoelectric properties of the material and their potential for application in thermoelectric devices.

Keywords: topological insulators, thermopower, quantum transport, HgTe quantum wells

G.M. Gusev [1, a], **Z.D. Kvon** [2, 3, b], **A.D. Levin** [1, c], **E.B. Olshanetsky** [2, 4, d], **N.N. Mikhailov** [2, e]
[1] Universidade de São Paulo, Instituto de Física, São Paulo, Brazil
[2] Rzhanov Institute of Semiconductor Physics, Siberian Branch of the Russian Academy of Sciences, prosp. Akademika Lavrenteva 13, 630090 Novosibirsk, Russian Federation
[3] Novosibirsk State University, Akademgorodok, ul. Pirogova 2, 630090 Novosibirsk, Russian Federation
[4] Novosibirsk State Technical University, prosp. Karl Marx 20, 630073 Novosibirsk, Russian Federation
E-mail: [a] gusev@if.usp.br, [b] kvon@isp.nsc.ru, [c] alexander.d.levin@gmail.com, [d] eolsh@isp.nsc.ru, [e] mikhailov@isp.nsc.ru

Received 14 February 2025, revised 2 April 2025
Uspekhi Fizicheskikh Nauk **196** (1) 2 – 27 (2026)
Translated by the authors

1. Introduction

Thermoelectric effects in solids belong to the class of fundamental kinetic phenomena [1]. They provide supplementary insight into electron transport in metals and semiconductors, which makes them a valuable tool for identifying the charge carriers and transport mechanisms at play. These effects also have a significant application value, being related to the transformation of the thermal form of energy into the electrical [2]. The recent discovery of topological insulators (TIs) and 2D classical and Weyl semimetals opens new prospects in this field, owing to their unconventional electronic structure and unique properties. TIs exhibit unique transport properties that stem from the gapless linear spectrum of their helical surface or edge states [3–12]. For instance, the edge states of two-dimensional TIs are theoretically expected to have an extremely large mean free path and mobility due to their protection against backscattering [3–5, 13–15]. In 2D TIs, the transport is determined by the edge states, when the Fermi level stays

within the insulating gap. The position of the Fermi level in the gap is stabilized by the bulk states present in the gap, arising from random spatial inhomogeneity or disorder. These states are typically localized, but electron transitions between the edge and bulk states are possible and may affect transport properties in 2D TIs. The mixing of edge and bulk states is thought to strongly enhance the diffusive thermopower in 2D TIs. 2D classical and Weyl semimetals are also novel and interesting kinds of 2D and 3D electron systems [16–20]. Two-component (electron-hole) classical and quantum transport, Landau electron-hole scattering, the quantum Hall effect in an electron-hole liquid, 2D networks of helical edge states — this is just an incomplete list of new physical phenomena discovered in these systems during the last two decades [17, 21].

It is necessary to note that, to date, HgTe has been the only semiconductor on whose basis 2D TI and 3D TI, 2D classical and Weyl semimetals, have been experimentally realized in the most reliable way. Therefore, there is no doubt that the investigation of their thermoelectric properties is a very important task of modern condensed matter physics.

Some recent review articles, including [22–25], are mostly focused on three-dimensional topological insulators and semimetals. They offer valuable insights into the latest research in the field and help to guide future research efforts aimed at developing more efficient energy conversion technologies. In contrast to them, this review article provides a comprehensive summary of the latest research on the thermoelectric properties of 2D topological insulators and semimetals based on HgTe material. It covers a range of topics, including the theoretical underpinnings concerning these materials, experimental methods of measuring their thermoelectric properties, and analysis of scattering mechanisms.

2. Energy spectrum of HgTe-based topological insulators and two-dimensional semimetals

In this section, we describe the energy spectrum of a quantum well (QW) and films based on HgTe in more detail. Figure 1 shows a qualitative view of the energies of the main dimensional-quantization subbands in such a well as a function of its thickness [26–28]. As can be seen, the behavior of the spectrum fundamentally depends on the well thickness, and it can be conventionally divided into four regions. The first is $d_w < d_c$, where a direct-band-gap 2D insulator is realized. Its band gap decreases as the thickness increases, to collapse at a critical well thickness d_c, which is equal to 6.3–6.5 nm, depending on the QW orientation and deformation. As d_w increases further, the second region appears, which contains a 2D insulator but with inverse bands. Then, if $14 < d_w < 30$ nm, a 2D semimetal state emerges due to the overlap of hole-like bands H_1 (conduction band) and H_2 (valence band). Finally, if $d_w \geqslant 60$ nm, we have a three-dimensional topological insulator.

Let us consider the energy spectrum of some of these systems in more detail, starting with a 2D TI. The energy spectrum of such a TI calculated in [29] for (100) and (013) surface orientations is shown in Fig. 2a. As can be seen, the basic characteristics of this spectrum depend only weakly on the surface orientation. The critical thickness in both cases is 6.3 nm, and the 2D TI state with the largest band gap, corresponding to simple band inversion, is realized at a QW thickness of 8.2–8.5 nm. The band gap width is in this case approximately 30 meV. The dispersion law for edge and bulk states for a QW with a thickness of 8.5 nm and orientation (013) is shown in Fig. 2b, which illustrates well all the features of the spectrum of a 2D TI based on the HgTe QW: the linear Dirac spectrum of edge current states and a parabolic band-gap spectrum of bulk states. We note that the edge states exist not only in the band gap but also at energies that correspond to the allowed bulk bands. Fig. 2b also clearly shows the anticrossing of the edge states with the bulk states in the lower part of the band gap due to lower surface symmetry (013).

Figure 2c presents the energy spectrum of an HgTe QW with critical thickness $d_w = 6.3-6.5$ nm at which a Weyl-like 2D semimetal emerges. According to the calculation carried out in many papers, the spectrum of an HgTe QW with $d = d_c$ represents a symmetric Dirac cone with the dispersion $E = \hbar v_{DF} k$ ($v_{DF} = 7-8 \times 10^7$ cm s^{-1}) in the vicinity of the Dirac point only, at energies lower than 20–30 meV. Some way down from the Dirac point, an additional extremum of heavy 2D holes appears at some point away from the center of the Brillouin zone.

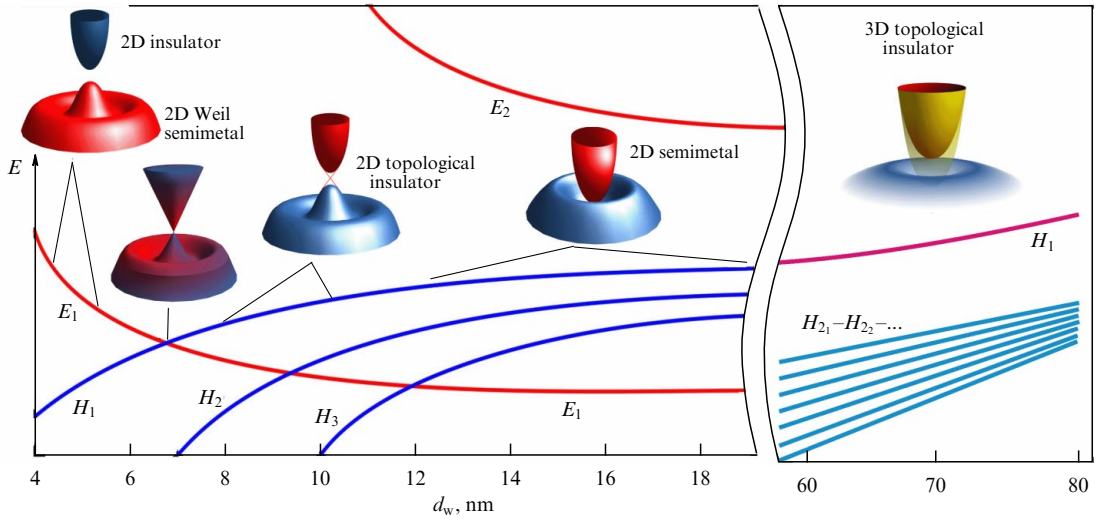

Figure 1. Qualitative view of energy spectrum of HgTe-based topological insulators and two-dimensional semimetal (E_1 and E_2 are energies of electron subband, H_1, H_2, and H_3 are energies of hole subband).

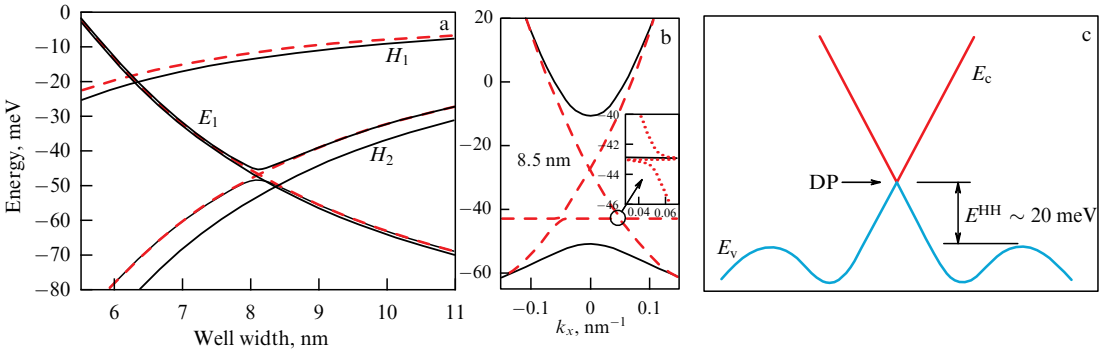

Figure 2. (a) Subband bottom energy as function of QW thickness in range of 5.5–11 nm (solid curves for surface orientation (100), dashed curves for orientation (013)). (b) Dispersion law of bulk and edge states for HgTe QWs with orientation (013). (Figure taken from [29].) (c) Qualitative view of energy spectrum in HgTe QW of critical width $d_w = 6.3-6.5$ nm.

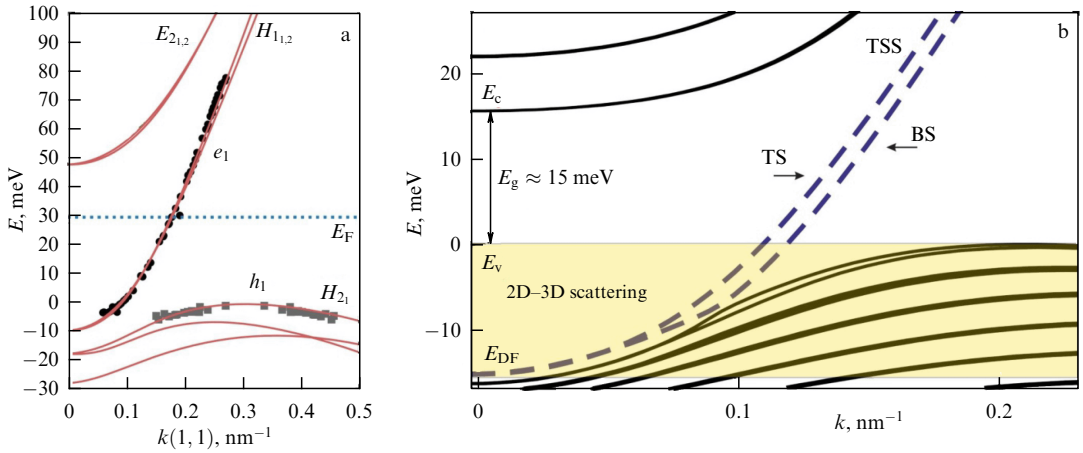

Figure 3. (a) Energy spectrum of 2D semimetal in HgTe QW ($d_w = 22$ nm). Symbols — experimental data obtained from cyclotron mass, solid lines — calculation by means of $k \times p$ model. (Figure taken from [30].) (b) Band structure of 3D topological insulator on basis of strained 80-nm HgTe film. Solid lines — bulk state energy dispersion, dashed lines — energy dispersion of surface Dirac fermions from top (TS) and bottom (BS) surfaces. Approximate energy window where surface electrons and bulk holes coexist is marked by yellow shading. (Figure taken from [31].)

Figure 3a shows the typical energy spectrum of a 2D semimetal in a QW with a thickness of 22 nm. It can be seen that we have a 2D semimetal with an overlap of about 10 meV between the CB minimum at the center of the Brillouin band and two valence band valleys in the [03-1] direction. The electron effective mass is $m_e = 0.025-0.03m_0$ and the hole mass $m_h = 0.25-0.3m_0$ is about ten times larger [30].

It is necessary to note that bulk mercury telluride, despite the inverted nature of its spectrum, cannot be classified as a TI because it is a gapless semiconductor. However, a transformation into a 3D TI state can occur if a uniaxial compression deformation is applied to HgTe that results in the bulk gap opening. A similar but not identical situation occurs in the case of HgTe films grown on CdTe substrates due to the difference in the lattice constants of HgTe ($a_{HgTe} = 0.646$ nm) and CdTe ($a_{CdTe} = 0.648$ nm). The critical thickness of pseudomorphic growth that corresponds to this difference in the lattice constants is more than 100 nm, and thus films whose thickness is less than this critical value reproduce the lattice constant of the CdTe substrate. As a result, tensile deformation occurring in such films leads to the emergence of a gap. However, the Dirac point in a TI created in this way is located not inside the band gap but deep in the valence band. Due to hybridization with the valence band, the spectrum of surface states contains only the electron branch, which, when approaching the valence band bottom, deviates from the linear law to become quasiparabolic. Figure 3b demonstrates the energy spectrum of a 3D topological insulator, realized in 80-nm HgTe [31]. It is clear that, as the energy increases, an indirect band gap of approximately 15 meV emerges in the bulk of the film, in which there are surface bands of delocalized electron states. Because the thickness of the film is finite, its spectrum in the allowed bulk bands consists of a sequence of dimensionally quantized subbands with a small (1 meV) distance between them in the valence band and with an order of magnitude larger separation in the conduction band.

3. Experimental setup

Quantum wells $Cd_{0.65}Hg_{0.35}Te/HgTe/Cd_{0.65}Hg_{0.35}Te$ with (013) surface orientations and a different nominal well thickness were prepared by molecular beam epitaxy. As shown in previous publications (see review [11]), the use of substrates inclined to singular orientations facilitates the growth of more perfect films. Therefore, the growth of alloys is performed predominantly on substrates with a surface orientation (013), which deviates from the singular orientation by approximately 19°. The original wafer containing the HgTe quantum well was patterned into experimental samples

Table 1. Sample parameters and configuration of Hall bar used for transport measurements.

Sample	d, nm	Hall bridge
2D topological insulator	8.1–8.3	Mesoscopic
3D topological insulator	80	Macroscopic
2D semimetal	21	Macroscopic
2D Weil semimetal	6.3–6.4	Macroscopic

of different configurations and sizes. Macroscopic samples with a 4 × 3-mm rectangular shape bore on top an ordinary Hall structure with $L \times W = 100 \times 50$ μm and 250 × 50-μm segments between the voltage probes prepared by photolithography and chemical etching. The mesoscopic structure was a long Hall bar consisting of three consecutive segments of different lengths (3, 9, and 35 μm) and seven voltage probes.

The fabrication of an ohmic contact to an HgTe quantum well is similar to that for other 2D systems, such as GaAs quantum wells: the contacts were formed by the burning-in of indium directly on the surface of large contact pads. Modulation-doped HgTe/CdHgTe quantum wells are typically grown at $T = 180°$ C, which is relatively low compared to $A_{III}-B_V$ compounds. On each contact pad, the indium diffuses vertically down, providing ohmic contact to the underlying quantum well, with contact resistance in the range of 0.1–1 kΩ. During AC measurements, we made sure that the Y-component of the impedance did not exceed 5% of the total impedance, which is an indication of good ohmicity of the contacts. A dielectric layer was deposited (100 nm of SiO_2 and 100 nm of Si_3Ni_4) on the sample surface and then covered by a TiAu gate. The density variation with the gate voltage was 10^{11} cm^{-2} V^{-1}. The magnetotransport measurements were performed at a temperature of 4.2 K using a standard four point circuit with a 1–13-Hz AC current of 1–10 nA through the sample, which is sufficiently low to avoid overheating effects. The thermoelectric power was measured as follows. At one end of the sample, close to one of the Hall bar current contacts, there was a heater, a thin metal strip with a resistance of ≈ 50 Ω. The opposite cold end of the sample was indium soldered to a 5-mm^3 copper piece, which, in turn, was brought in thermal contact with the massive copper sample holder. To create a temperature gradient along the Hall bar, an alternating current not exceeding 60 mA and with a frequency of 0.4–1 Hz was passed through the heater. For the current range specified, the heater functioned in a linear regime. A schematic of sample form thermopower measurements is depicted in Fig. 4.

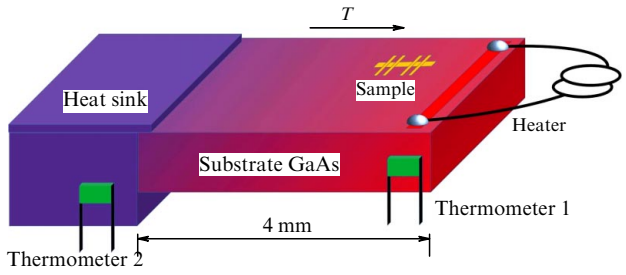

Figure 4. Schematic of sample for thermopower measurements.

To control the temperature gradient along the sample, two calibrated thermistors were used — one located at the heater end and the other at the cold end of the sample. For example, the temperature difference thus determined between the voltage contacts 100 μm apart at ambient temperature $T = 4.2$ K and $V_{p-p}^{heater} = 6$ V was $\Delta T \approx 0.023$ K or, equivalently, $\nabla T = 230$ K m^{-1}. In the operating temperature range ($\approx 2.2 - 4.2$ K), the thermal conductivity of liquid helium is negligible compared to phonon thermal conductivity of the wafer substrate. In these conditions, it is the thermal conductivity of the substrate that determines the temperature gradient along the sample. The thermopower signal was measured at a double frequency using available voltage contacts. The experimentally measured quantities for macroscopic Hall bars were the longitudinal thermovoltage $V_{xx} = S_{xx}\nabla T \times L$, where $L = 450$ or 100 μm is the distance between the voltage probes along the temperature gradient ∇T, and the transverse thermovoltage $V_{xy} = S_{xy}\nabla T \times W$, where $W = 50$ μm is the sample width normal to the temperature gradient. From V_{xx} and V_{xy} thus obtained, the Seebeck S_{xx} coefficient could be evaluated for comparison with theory. For mesoscopic samples, we did not directly measure the temperature difference between the voltage probes due to the small distance, but we estimated the gradient $\nabla T \sim 160 - 230$ K m^{-1} for the heater power used in our experiment.

4. Thermopower 2D topological insulator

4.1 Theoretical model

In the 2D band transport, phonon drag in HgTe wells appears to be much less important than in GaAs wells because of the relative smallness of deformation-potential and piezoelectric constants in HgTe, and also because of the smallness of the density of states of the 2D carriers (in other words, the smallness of the effective mass, as the drag thermopower is proportional to the square of this mass). By order of value, the phonon drag thermopower in HgTe can be comparable to diffusive thermopower in the temperature range of 2–4.2 K. However, calculations show that, for this mechanism, the density and temperature dependences of thermopower are different from those observed in experiment. One can assume that the phonon drag thermopower increases with $V_g - V_{CNP}$ up to high densities of 10^{12} cm^{-2}; therefore, it can be important in 2D semimetals and 3D HgTe-based topological insulators. We consider this contribution in other chapters devoted to HgTe semimetal.

Phonon drag for edge states is not considered, because large momentum transfer from phonons to electrons requires spin-flip phonon-assisted backscattering between edge states propagating in opposite directions. This scattering has a very low probability. Therefore, below, we focus on the diffusive thermopower.

In paper [32], the authors suggest that an extremely high $ZT > 2$ can be realized in a 2D topological insulator. Such enhancement of ZT is mainly due to the dramatic difference in the relaxation time between the backscattering-free in-gap topological edge states and the highly scattering 2D bulk states. Assuming that the Fermi level is situated near the bottom of the conduction band, as illustrated in Fig. 5a, the relaxation time of high-energy electrons decreases due to the scattering into the bulk conduction band. Moreover, it is expected that the scattering between edge states is forbidden

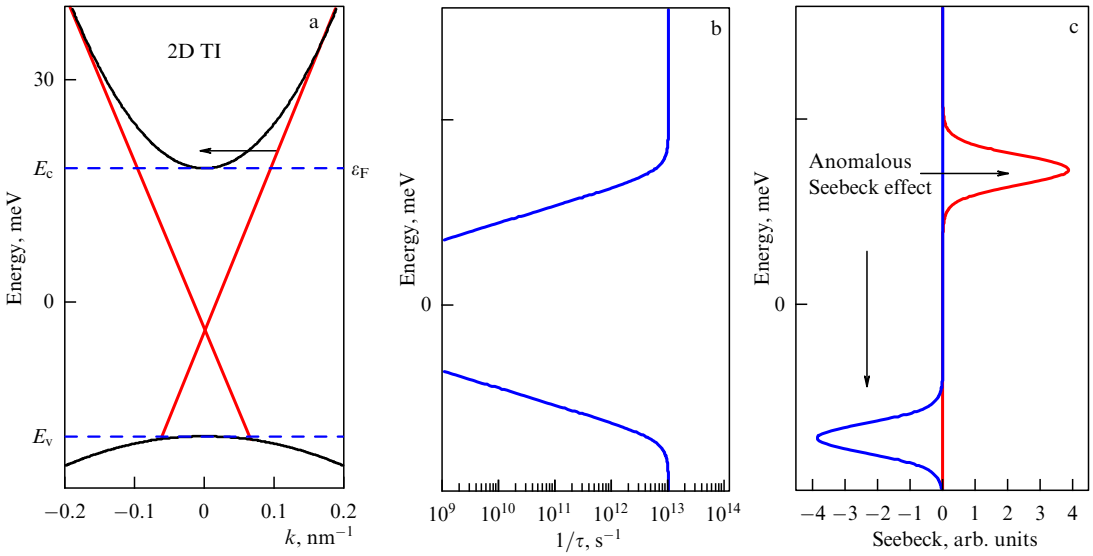

Figure 5. (a) Schematic of topological edge states and bulk bands. Conduction and valence band edges are marked by E_c and E_v. When Fermi level is located near bottom of conduction band, electrons with energy $\varepsilon > E_c$ can be scattered into bulk states. (b) Relaxation rate of edge state electrons as function of energy. (c) Seebeck coefficient as function of energy.

due to time inverse symmetry protection. If there is a significant difference between the relaxation times of Dirac fermions occupying edge states above and below the Fermi level (Fig. 5b), then the thermoelectric power of the system can change sign and become positive (anomalous sign), as shown in Fig. 5c. Furthermore, the magnitude of this effect can be much larger than that observed in the absence of selective scattering.

However, note that this mechanism requires the complete suppression of scattering between the edge states, which is not observed in realistic structures. The quantized conductance of HgTe-based quantum wells exhibits significant deviation from the value h/e^2 in the long samples [11, 33] predicted by the Landauer–Buttiker formalism. This deviation from the theoretical predictions has been attributed to various factors, such as disorder, the presence of charge puddles, and numerous sources of inelastic scattering [34–53].

When the regime deviates from the ballistic one, it is reasonable to assume that the scattering of edge states into the bulk must be taken into account, in addition to backscattering between them. In such cases, the Landauer–Buttiker formalism is inadequate for quantitative analysis. To address this problem, two phenomenological parameters, γ and g, can be introduced to represent the rate of scattering between edge states and between edge states and the bulk. The scattering between the edge and bulk states becomes significant when the Fermi level lies within the conduction or valence bands (see Fig. 5a), while it can be negligible when the Fermi level crosses the band gap. In order to determine the bulk conductivity, electron and hole bulk densities, and to study transport properties, it is crucial to consider the density of states. One can argue here that the conduction and valence bands have Gaussian tails that stretch into the band gap due to the random potential. Although the electrons and holes in the band tails should be localized according to the generally accepted theory, for simplicity, we assume a finite residual conductivity in the band tails to explain the reduction of nonlocal transport near the charge neutrality point (CNP).

The local and nonlocal transport coefficients depend on the contribution of the edge states and the short-circuiting of the edge transport by the bulk contribution, with the latter being more significant away from the CNP. A comparison of local conductance and nonlocal resistance [54] demonstrates the range of voltages where edge state transport dominates. The nonlocal signal is zero when the Fermi level lies within the conduction or valence bands, far away from the CNP, or when the classical model predicts negligible nonlocal resistance. As the gate voltage sweeps through the CNP, transitions occur between the edge states and the electron and hole bulk states, allowing us to study the intermediate situation that corresponds to a mixture of the edge and bulk contributions to the conductance.

Papers [55, 56] present the edge + bulk model, which accounts for the mixing between the edge and bulk states when the Fermi level crosses the energy gap. This model has been developed to describe the behavior of conductivity and thermopower [56] in two-dimensional topological insulators.

For simplicity, we considered that the 2D band model with a Dirac Hamiltonian leads to a symmetric energy spectrum of electrons and holes separated by the gap Δ, $\varepsilon = \pm\varepsilon_k$, $\varepsilon_k = [\Delta^2/4 + A^2k^2]^{1/2}$, where $A = 360$ meV $\times$ nm and $\Delta = 36$ meV. In a realistic case, the spectrum is not symmetric [29]: the electron and hole effective masses have been obtained from cyclotron resonance experiments. The values are $m_e \approx 0.02m_0$ and $m_h \approx 0.2m_0$, respectively, and found to be energy dependent due to non parabolicity. Therefore, the bulk conductivity σ_b can be expressed by the equation

$$\sigma_b(\varepsilon) = \frac{e^2 v_F^2 \tau(\varepsilon) D(\varepsilon)}{2}, \qquad (1)$$

where $D(\varepsilon)$ is the density of states, and v_F is the Fermi velocity. We introduce $\tilde{\sigma} = \sigma_b/(e^2/h)$. Assuming that the scattering of carriers is caused by impurities or other inhomogeneities with short-range potentials described by the momentum-independent correlator d, the scattering rate is found as

$$\frac{1}{\tau(\varepsilon)} = \frac{d}{\hbar A^2}\left(\frac{\varepsilon + \Delta^2}{4\varepsilon}\right). \qquad (2)$$

The edge + bulk model for thermopower predicts the following contributions to the conductance and thermopower [56]:

$$G_e = \frac{e^2}{h}\,\mathcal{F}^{-1}\,,\quad \mathcal{F} = 1 + \gamma L + \frac{(L/w)\tilde{\sigma} g L}{(2L/w)\tilde{\sigma} + gL}\,, \tag{3}$$

$$S_e = \frac{\pi^2}{3}\,\frac{k_B}{|e|}\,(k_B T)\,\frac{\mathcal{F}'}{\mathcal{F}}\,, \tag{4}$$

$$S_b = \frac{\pi^2}{3}\,\frac{k_B}{|e|}\,(k_B T)\,\frac{G_b'}{G_b}\,, \tag{5}$$

while the total conductance and thermopower are

$$G_{tot} = 2(G_e + G_b)\,,\quad S_{tot} = \frac{S_e G_e + S_b G_b}{G_e + G_b}\,, \tag{6}$$

where $G_b = \sigma w/L = (e^2/h)(w/L)\tilde{\sigma}$ is the bulk conductance per spin, and k_B is a Boltzmann constant. Though the theory leading to Eqns (3)–(5) initially assumes $gL \gg 1$, these equations remain formally valid in the opposite limit $gL \ll 1$, when the edge state contribution to the conductance is not influenced by the bulk-edge currents and $G_e = e^2/h(1+\gamma L)^{-1}$. This means that Eqns (3)–(5) can be used as a reasonable approximation for arbitrary gL.

The main results of our theoretical model are given by Equations (3)–(5), which show that the function $\mathcal{F}$ contains two terms: the first depends on the scattering between edges, while the second describes the edge-to-bulk leakage.

Two cases can be considered:

(1) The Fermi level lies within the energy gap. In this case, if the bulk transport is suppressed by localization, the backscattering between the edge states governs the behavior of the conductance and thermopower.

(2) The Fermi level crosses the conduction (or valence) band. The edge state conductance and thermopower are determined by Equations (3) and (4). If $(L/w)\tilde{\sigma} \ll gL$, the presence of the edge to bulk scattering does not strongly affect either the resistance or the thermopower, because

$$\mathcal{F} = 1 + \gamma L + \frac{L}{w}\,\tilde{\sigma}\,.$$

This also means that, even when energy dependence of g is strong, the thermopower sign alteration considered in model [32] does not occur. For a long narrow sample and for high mobility bulk carriers (high conductivity), if $(L/w)\tilde{\sigma} \gg gL$, the edge state contribution to function $\mathcal{F}$ should be proportional to gL, and the conductance and thermopower should be given by

$$G = \frac{e^2}{h}\,(1 + \gamma L + g)^{-1}\,,$$

$$S = \left(\frac{\pi^2}{3}\,\frac{k_B}{|e|}\,(k_B T)\right)\,\frac{\gamma' + g'}{1 + \gamma L + gL}\,,$$

where γ' and g' stand for the derivatives of γ and g with respect to energy. Note that, for the limiting case $\gamma' \ll g' \ll 0$, the thermopower is large and has a positive anomalous sign for electrons (for conventional 2D and 3D systems, the Seebeck coefficient is always negative for electrons). This mechanism was predicted in model [32].

In the case of ballistic transport, the contribution of edge states to thermopower is expected to be absent. Typically, the backscattering rate γ is expected to be a smooth function of the chemical potential, decreasing monotonically away from the CNP. This is because the CNP corresponds to the crossing point in the edge-state spectrum, where the transferred momentum is zero and the elastic scattering rate usually decreases with increasing transferred momentum. As a result, the resistance decreases with gate voltage $V_g - V_{CNP}$, and the thermopower has a negative slope near the CNP, as observed in experiments. If we count the energy from the Dirac point, the transferred momentum is given by

$$\gamma(\varepsilon) = \frac{\gamma_0}{1 + (\varepsilon/\varepsilon_0)^2}\,.$$

One can find $\gamma'/\gamma = -(2\varepsilon/\varepsilon_0^2)/[1 + (\varepsilon/\varepsilon_0)^2]$, where γ_0 is the scattering rate at zero energy and ε_0 is a characteristic parameter for energy smoothing. In the region near the CNP, where the transport is dominated by the edge states, the thermopower is a linear function of the Fermi energy. It is negative in the electron part and positive in the hole part. Therefore, the slope of the thermopower near the CNP is entirely determined by the energy dependence of the backscattering rate.

Our findings suggest that bulk transport plays an essential role in our samples, even in the vicinity of the CNP. Although we observed a considerable nonlocal resistance indicating edge transport, the persistence of bulk electron transport suggests that our samples have a high level of disorder. As a result, the bulk component of conductance persists throughout the gate voltage range, even within the gap region. These results highlight the importance of considering bulk transport in the analysis of our samples, despite the presence of edge transport. As we already mentioned above, one would expect a significant increase in the edge-to-bulk scattering rate near E_c or E_v (Fig. 3b). We assume

$$g(\varepsilon) = \frac{g_0}{\exp\left[-(\varepsilon - \Delta/2)/2\varepsilon_0\right] + 1} + g_b\,,$$

where g_0 and g_b are the scattering rates at infinite and zero energy.

As previously mentioned, when the sample is narrow and long and $(L/w)\tilde{\sigma} \gg gL$, both γ' and g' contribute equally to the transport properties. However, the observation of nonlocal resistance [15, 54, 57] provides clear evidence of edge state transport within the mobility gap ($-1.5V < V_g < 1.5V$). Assuming $gL \sim \gamma L \sim 1$, the mixing between edge states and the bulk becomes significant for probes 3–2 ($L/w = 10$) when the bulk conductivity is $\sigma \gg 0.1e^2/h$. According to our model (Ref. [55]), the estimated value of the bulk conductivity is $\sim 0.08e^2/h$.

The qualitative dependence of the thermopower observed in experiments is reproduced by any physically reasonable model of the density of states. For instance, the use of a Lorentzian spectral function to account for the broadening of electron states leads to the following equation:

$$D_\varepsilon = \frac{1}{\pi A^2}\left[\varepsilon \tan\frac{\varepsilon - \Delta/2}{\delta} + \beta\varepsilon \tan\frac{\varepsilon + \Delta/2}{\delta} + \frac{1}{2}\,\delta C_\varepsilon\right], \tag{7}$$

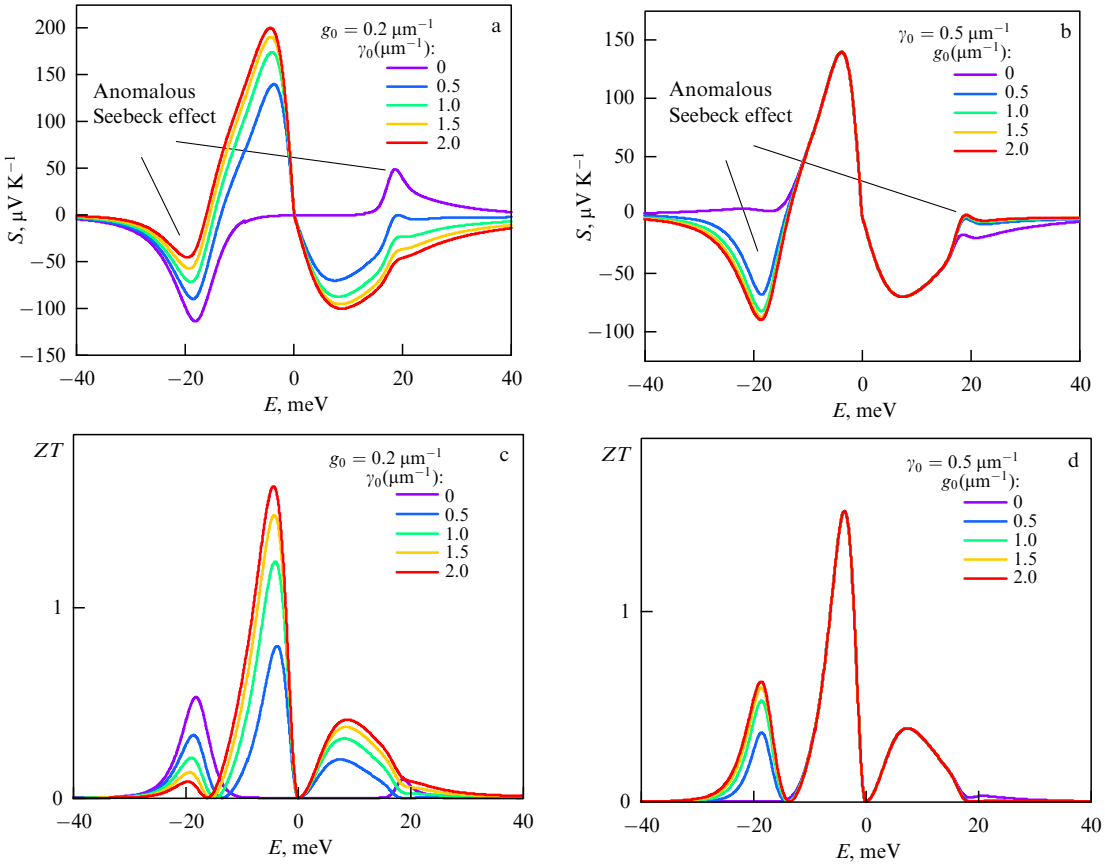

Figure 6. Diffusive thermopower calculated from Eqns (3) and (5) as function of Fermi energy for different scattering parameters, $L = 5$ μm, $T = 4.2$ K: (a) edge-to-bulk scattering parameter g_0 is fixed, while edge-to-edge scattering parameter γ_0 is varied, (b) edge-to-edge scattering parameter γ_0 is fixed, while edge-to-bulk scattering parameter g_0 is varied. Corresponding figure of merit ZT as function of Fermi energy for different scattering parameters, $L = 5$ μm, $T = 4.2$ K: (c) edge-to-bulk scattering parameter g_0 is fixed, while edge-to-edge scattering parameter γ_0 is varied, (d) edge-to-edge scattering parameter γ_0 is fixed, while edge-to-bulk scattering parameter g_0 is varied.

where

$$C_\varepsilon = \ln\left(\frac{(\varepsilon - E_c)^2 + \delta^2}{(\varepsilon - \Delta/2)^2 + \delta^2}\right) + \ln\left(\frac{(\varepsilon + E_c)^2 + \delta^2}{(\varepsilon + \Delta/2)^2 + \delta^2}\right), \quad (8)$$

δ is the broadening energy, and E_c is a large cutoff energy. In the hole region ($\varepsilon < 0$), the extra coefficient $\beta \approx 6$ is added, and the density of band states is larger.

Figure 6a shows the thermopower calculated from equations (3)–(8) taking into account the Lorentzian energy dependence of the backscattering rate for different parameters γ_0 with the following parameters: $E_c = 150$ meV, $\delta = 6$ meV, $\beta = 6$, $g_b = 0.1$ μm^{-1}, $\epsilon_0 = 10$ meV. Edge-to-bulk scattering is fixed. One can see the peak in the thermopower signal, when the chemical potential approaches the valence and conductance band edges. The thermopower has an anomalous signal: negative for holes and positive for electrons, as predicted in model [32]. Figure 6b displays the thermopower for various values of g_0, with fixed edge-to-edge scattering. It is evident from the figure that the thermopower within the gap remains constant, since the scattering between the edges remains unchanged.

The Wiedemann–Franz law dictates that the electronic thermal conductivity of the quantum well should be relatively high, while the lattice thermal conductivity can be reduced due to phonon scattering. As a result, rough estimates can be performed by ignoring the lattice thermal conductivity. We can express the dimensionless figure of merit:

$$ZT = \frac{S^2\sigma}{\kappa}T = \frac{3}{\pi^2}\left(\frac{S}{k_B/e}\right)^2.$$

In edge state heating experiments [58], the validity of the Lorentz ratio has been tested and it has been found that the Wiedmann–Franz law applies to both the edge states and bulk transport regime. It's important to note that, in our current analysis, we haven't considered the thermal conductivity of the substrate. However, in real-world scenarios, the substrate can have a significant impact on the overall thermoelectric conductivity. Figure 6 c, d displays the figure of merit for various values of γ_0 (c) and g_0 (d), consequently, with fixed edge-to-bulk (edge to edge) scattering. It can be seen that ZT can be dramatically enhanced up to ~ 1.6 due to strong energy dependence of the parameter $\gamma(\varepsilon)$. This is a reasonable assumption, supported by recent studies that have reviewed various backscattering mechanisms invoked to explain the scattering between topologically protected states [33]. It should be noted that the energy dependence of the parameter $g(\varepsilon)$ (which accounts for edge-to-bulk scattering) can significantly enhance the thermoelectric efficiency. By fine-tuning this dependence, it is possible to achieve similar values of ZT. Figure 7a, b depicts the thermopower (a) and figure of merit (b) for various sample lengths while keeping the parameters γ_0 (c) and g_0 (d) fixed. To minimize the anomalous Seebeck effect resulting from extensive mixing

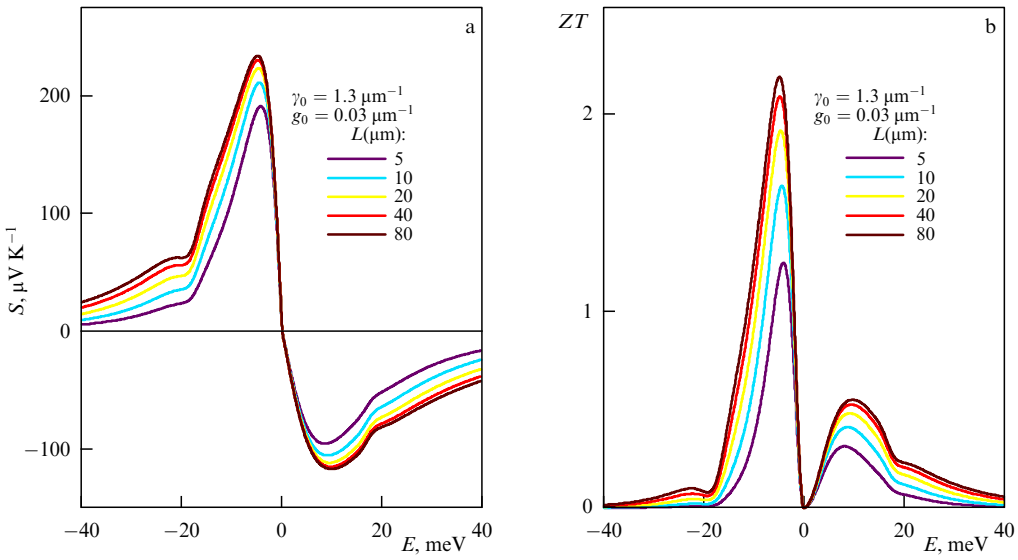

Figure 7. (a) Diffusive thermopower calculated from equations (3) and (5) as function of Fermi energy for sample length L, $T = 4.2$ K. (b) Corresponding figure of merit ZT as function of Fermi energy for different sample length, $T = 4.2$ K.

between the edge and bulk, we opted for a small edge-to-bulk scattering parameter. The saturation of the thermopower signal with device length can be seen. To summarize, the Seebeck coefficient changes sign due to strong selective scattering. This results in partial thermoelectric powers due to edge-to-edge and edge-to-bulk scattering having different signs and largely offsetting each other. Additionally, the maximum thermoelectric figures of merit differ when only edge-to-edge and edge-to-bulk scattering are present, and are reached at different chemical potential values. If there are multiple scattering channels with varying thermoelectric properties, the efficiency of the entire electronic system may be less than the largest partial efficiency.

4.2 Discussion and comparison with experiment

The experimental setup and methods for the resistance and the thermopower measurements have been described in the previous section. Four different mesoscopic devices were studied, and the results obtained in two representative samples (A and B) are presented.

The variation in resistance with gate voltage and lattice (bath) temperature for two different samples (samples A and B) is shown in Fig. 8. The shortest segment of sample A exhibits a broad peak in resistance, with an amplitude larger than the expected value of $h/2e^2$ in the ballistic case. As the sample length increases, the resistance also increases, consistent with the diffusive case. In the case of sample B, we

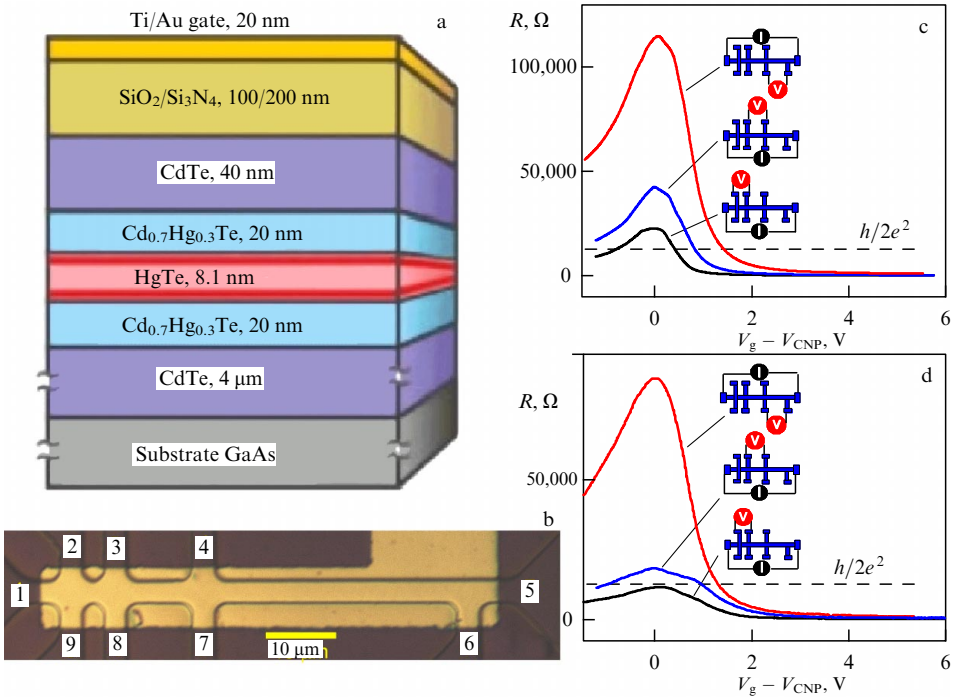

Figure 8. (a) Schematic of transistor and top view of sample. (b) Resistance at $T = 4.2$ K as function of gate voltage V_g for different configurations of measurements and for different devices (Samples A (c) and B (d)).

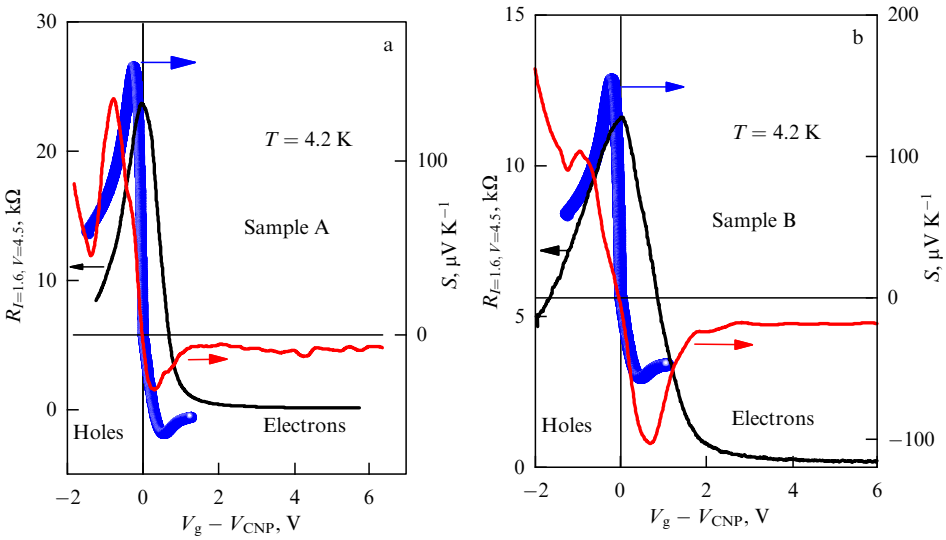

Figure 9. (a) Sample geometry. (b) Resistance and thermovoltage as function of gate voltage, $T = 4.2$ K, sample A (a) and sample B (b). Blue dots show theory calculated from Eqns (3)–(9) with parameters indicated in text (edge + bulk model).

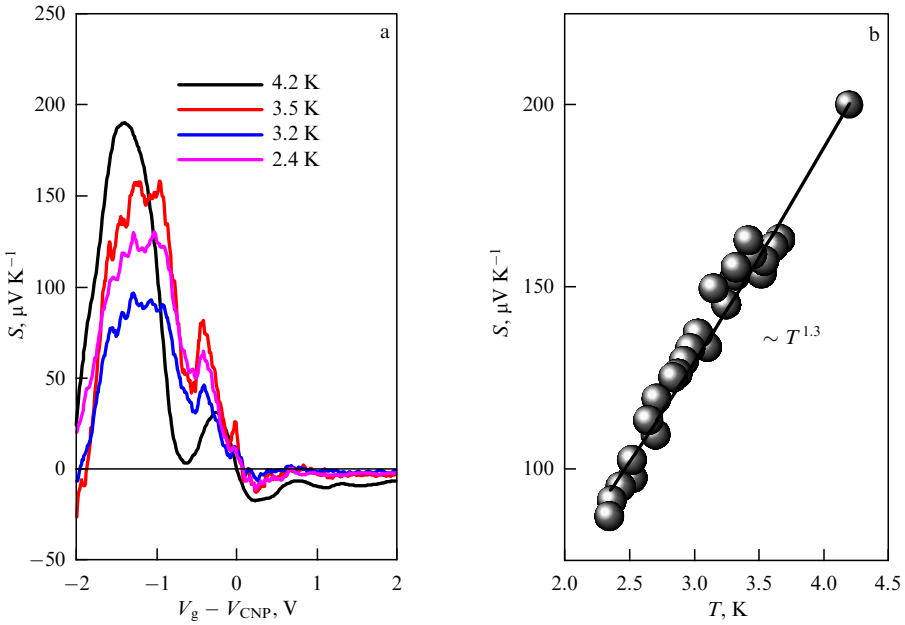

Figure 10. (a) Thermopower for different temperatures (Sample A). (b) Temperature dependence of thermopower at $V_g - V_{CNP} = -1.2$ V.

observe ballistic behavior for the resistance between contacts 2–3 (9–8), with the resistance approaching the quantized value of $h/2e^2$ (see Fig. 8d). However, it is important to note that the resistance increases with probe distance, indicating strong edge-to-edge scattering. We have also measured the temperature dependence of the curves $R(V_g)$ and observed that the resistance decreases sharply for temperatures above 15 K and saturates below 10 K [59]. The profile of the resistance-temperature dependences at $T > 15$ K fits well with the activation law $R \sim \exp(\Delta/2kT)$, where Δ is the activation gap. The thermally activated behavior of resistance above 15 K corresponds to a gap of 10 meV between the conduction and valence bands in the HgTe well. The mobility gap can be smaller than the energy gap due to disorder.

Figure 9a, b shows the resistance and thermovoltage as a function of the gate voltage measured between probes 4 and 5 at $T = 4.2$ K for both samples. We find that the thermovoltage increases almost linearly with heater power, indicating that we measured the longitudinal (Seebeck) thermoelectric effect. The signal exhibits an ambipolar behavior similar to other electron-hole systems such as graphene. It changes sign at the CNP and decreases with increasing carrier density. The voltage interval between the electron-like and hole-like regimes ($\Delta V_g \sim 1$ V) is about one half the half-width of the resistance peak. Figure 10a displays the traces of thermopower versus V_g at different temperatures, while Fig. 10b shows the temperature dependence of the thermopower measured across a longer bridge at a selected gate voltage $V_g - V_{CNP} = -1.2$ V (hole side) where the thermopower approaches its maximum. It is worth noting that the temperature interval $2.2 < T < 4.2$ K was selected because resistance becomes temperature dependent at $T > 10$ K, and the metallic approximation for thermopower is no longer valid. The signal grows almost linearly with temperature in this interval, with $S \sim T^{1.3\pm0.1}$ (Fig. 10b). Prior to the thermoelectric measurements, the thermal conductance of

the sample was determined, and it was found that the thermoconductance is dominated by phonon transport in the substrate, with the contribution from the diffusive heat transfer by electrons being negligibly small. The thermal conductivity of the GaAs substrate is usually determined by the boundary scattering at low temperatures and can be calculated using following equation:

$$\kappa = \frac{2\pi^2}{15}\frac{k\Lambda}{v_{\mathrm{ph}}^2}\left(\frac{kT}{h}\right)^3,$$

where Λ is the phonon mean-free path, and $v_{\mathrm{ph}} = 3300\ \mathrm{m\ s^{-1}}$ is the appropriate mean acoustic phonon velocity. We determined the value of κ to be approximately $600\ \mathrm{W\ m^{-1}\,K^{-1}}$ at a temperature of 4.2 K, which is consistent with the previously measured thermal conductivity of pure GaAs substrate. To calculate the thermopower of our system, we employ Eqns (2)–(6) based on the bulk + edge model. However, it is important to note that we cannot simply translate the energy dependence to the density dependence, because the Fermi energy does not vary linearly with the number of states in the bulk gap region (n_s). Without any disorder, the chemical potential μ would jump from the conduction to the valence band, resulting in a sharp resistance peak rather than the broad maximum observed in the experiment. To account for this, we need to calculate the dependence of μ on n_s and p_s using the equations

$$n_s = \int_0^\infty D_\varepsilon(\varepsilon)\left(1+\exp\left(\frac{\varepsilon-\mu}{kT}\right)\right)^{-1}\mathrm{d}\varepsilon,$$

$$p_s = \int_{-\infty}^0 D_\varepsilon(\varepsilon)\left(1+\exp\left(-\frac{\varepsilon-\mu}{kT}\right)\right)^{-1}\mathrm{d}\varepsilon.$$

Equations (7)–(8) provide us with the density of states, $D_\varepsilon(\varepsilon)$. To calculate the thermopower, we use these equations along with the parameters $\gamma_0 = 1.3\ \mu\mathrm{m}^{-1}$ and $g_0 = 0.03\ \mu\mathrm{m}^{-1}$, as shown in Fig. 7. Parameters for the density of states are $E_c = 150$ meV, $\delta = 6$ meV, $\beta = 6$, $g_b = 0.1\ \mu\mathrm{m}^{-1}$, $\varepsilon_0 = 10$ meV. In the hole region ($\varepsilon < 0$), we add an extra coefficient $\epsilon_0 = 16$ meV for energy smoothing in the hole region. This calculation is in reasonable agreement with experiment in the region close to the CNP. It is evident that the calculated thermopower for bulk electrons exceeds the experimental values. This overestimation is attributed to the assumption of a linear energy dependence of the density of states, which is likely inaccurate far from the charge neutrality point.

Figure 11 presents a summary of the diffusive thermopower as a function of density for different proposals considered by the theory. The aim of this figure is to demonstrate how different features of the model affect the Seebeck coefficient. Figure 11a depicts the anomalous Seebeck effect proposed for the ideal case of helical topologically protected edge states, where a significant increase in the edge-to-bulk scattering rate near E_c or E_v occurs [32]. One can observe an anomalous opposite sign for electron and hole thermopower near the band edges. Figure 10b shows the Seebeck effect calculated with the assumption of the presence of strong helical states mixing and the absence of edge-to-bulk scattering. In this case, the thermopower demonstrates ambipolar behavior, which is similar to our observations. Figure 10c displays a more realistic case where both mechanisms of scattering (helical state mixing and leaking from the edge to the bulk) are considered. One can see that the edge + bulk model successfully reproduces the key features of the thermopower. This is significant, because it provides a theoretical framework for understanding the behavior of the thermopower in this system. However, it should be noted that our model relies on a strong energy dependence of the edge-to-edge scattering, which may not be present in a purely ballistic case.

As we already mentioned in the previous sections, the HgTe samples exhibit a nonlocal resistance, indicating the presence of edge transport, but bulk transport also appears to be important, even in the vicinity of the CNP. This suggests that our samples have a significant disorder level, resulting in the persistence of bulk electron transport even inside the gap, such that the bulk component of the conductance exists in the entire gate voltage range. Although the bulk transport may be of the hopping variety near the center of the gap, we do not see an exponential temperature dependence like $R \sim \exp\left[(T_c/T)^{1/3}\right]$, which corresponds to the Mott law for 2D carriers, because the bulk conductivity is short-circuited by the edge states.

However, the temperature behavior of the bulk thermopower is not expected to change significantly upon transition from band transport to hopping transport. For the band transport, $S_b \sim T$, whereas, for hopping transport, the thermopower was calculated in [60]. Applied to 2D electrons, the result of [60] can be written as

$$S_b = -\frac{\lambda}{e}\left[\frac{\pi-2}{\pi}\left(T^2T_c\right)^{1/3} + \frac{2\pi}{3}T\right]\left(\frac{\mathrm{d}\ln D_\varepsilon(\varepsilon)}{\mathrm{d}\varepsilon}\right). \quad (9)$$

Equation (9) describes the behavior of the thermopower S_b in a disordered system. The first term in the equation represents the contribution from the Mott law, which depends on a numerical constant λ, the density of states $1/D_\varepsilon(\varepsilon)a_0^2$, and a characteristic temperature T_c that scales inversely with the product of the density of states, the carrier mobility μ, and the square of the localization length a_0 of the electron wavefunction. The second term accounts for the weak localization correction to the Mott law, which becomes dominant in the regime close to the onset of band transport when the localization length becomes large and T_c is of the same order or smaller than T. Therefore, in this regime, the second term is the only relevant contribution to the thermopower, and S_b is proportional to T.

By using Eqn (9) with a scaling constant λ approximately equal to 1, it is possible to generate a graph of the thermopower in the hopping transport regime, which is depicted in Fig. 11d. This computation reasonably agrees with experimental results in the vicinity of the CNP. However, the numerical constant is closer to that of the metallic case. It is worth noting that neither hopping nor metallic transport models are expected to be reliable in this intermediate regime. Nonetheless, it is essential to gain insight into how the thermopower can vary with the electron density around the CNP. Moreover, to achieve a better match between the experimental outcomes and Eqn (9), it is necessary to have precise knowledge of the bulk conductivity behavior in both the gap and hole-side regions. It should be noted that the thermopower coefficient calculated for both the edge and edge + bulk models (Fig. 11a, b, and c) shows a dependence on the sample length, which is also observed in the experiment (Fig. 11e). However, the pure bulk model does not exhibit this

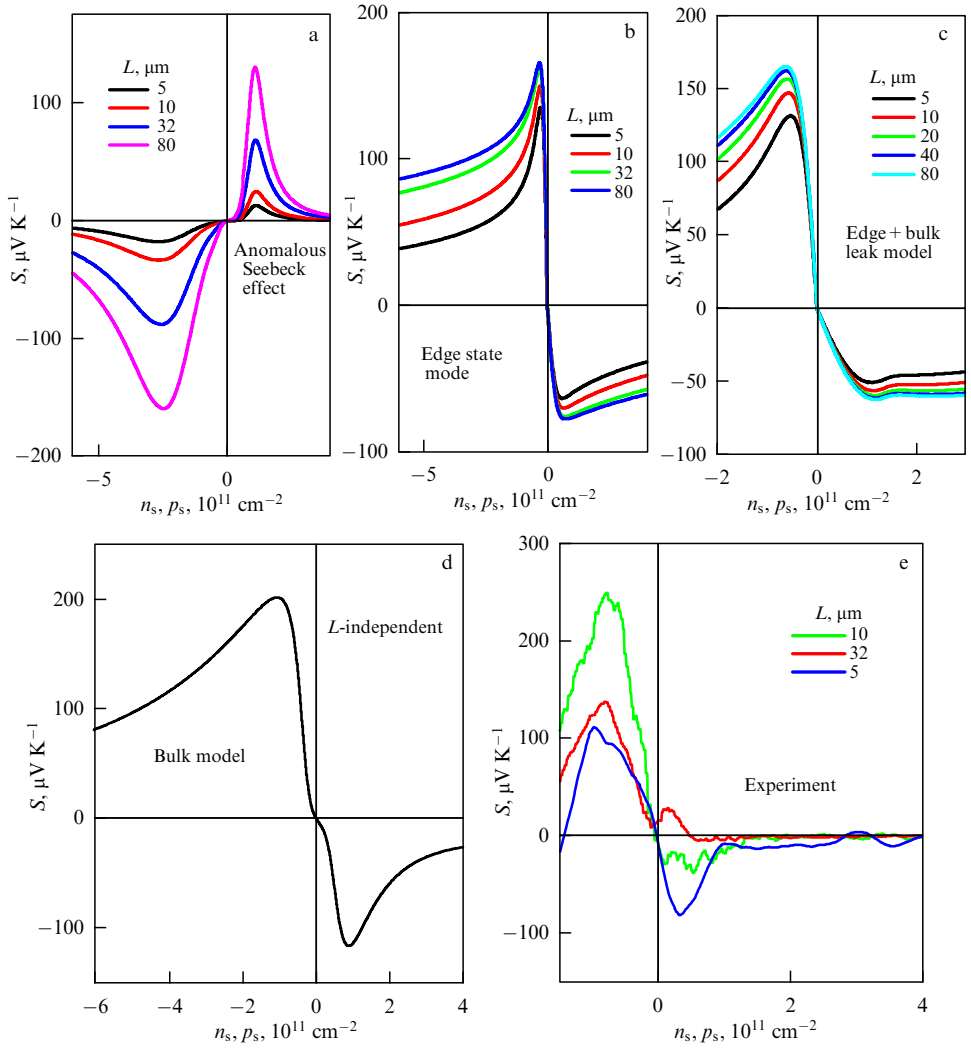

Figure 11. Comparison of different models for thermopower. (a) Diffusive thermopower calculated from Eqns (3)–(8) as function density for different sample length L, $T = 4.2$ K: $\gamma_0 = 0$ μm^{-1}, and $g_0 = 0.03$ μm^{-1}. (b) Diffusive thermopower calculated from Eqns (3)–(8) as function density for different sample length L, $T = 4.2$ K: $\gamma_0 = 1.6$ μm^{-1}, and $g_0 = 0$ μm^{-1}. (c) Diffusive thermopower calculated from Eqns (3)–(8) as function density for different sample length L, $T = 4.2$ K: $\gamma_0 = 1.3$ μm^{-1}, and $g_0 = 0.03$ μm^{-1}. (d) Diffusive thermopower calculated from Eqn (9) as function density. Parameters for density of states are $E_c = 150$ meV, $\delta = 6$ meV, $\beta = 6$, $g_b = 0.1$ μm^{-1}, $\varepsilon_0 = 10$. In hole region ($\varepsilon < 0$), we add extra coefficient $\epsilon_0 = 16$ meV for energy smoothing in hole region. (e) Thermopower as function of gate voltage measured between various voltage probes with different lengths, $T = 4.2$ K.

behavior. It is important to note that our samples only exhibit ballistic behavior for small distances between probes, so the observed length dependence could be due to the transition between different transport regimes.

To summarize, when the Fermi level falls within the energy gap near the CNP, the resistance of the sample is typically comparable to or greater than $h/2e^2$. At this point, the sample is likely to be localized, with edge transport being the dominant factor influencing resistance. Conversely, when the Fermi level is away from the CNP, bulk diffusive transport tends to be the primary mechanism at play.

Interestingly, the thermopower of the sample appears to be largely determined by bulk properties, regardless of the position of the Fermi level. However, recent theoretical studies have suggested that there may be strong enhancements and sign variations in the thermopower as the system transitions from a localized state to a conducting one. Our theory of a thermoelectric response in 2D TIs accounts for the absence of such anomalies and supports the idea that the observed thermopower is primarily of bulk origin.

4.3 Conclusion

Currently, there is no definitive experimental evidence to support the claim that topological edge states significantly enhance the efficiency of thermoelectric materials. While theoretical calculations of the dimensionless thermoelectric efficiency have produced results ranging from values of ZT less than unity to values that are about an order of magnitude larger than those of ordinary bulk thermoelectrics, these results are based on several assumptions, such as a strong dependence of the edge-to-edge or edge-to-bulk leak on the energy. Therefore, it is doubtful whether the contribution of topological helical states of TIs can indeed multiply the thermoelectric efficiency as claimed. After analyzing the experimental data and conducting theoretical analysis, we have concluded that the observed thermopower is primarily of bulk origin or results from a strong energy dependence of the edge-to-edge leak. On the other hand, both edge and bulk transport contribute to the resistance.

5. Thermopower in 3D topological insulator

5.1 Introduction

A three-dimensional topological insulator (3D TI) is characterized by having gapless surface states inside the bulk band gap [3–5]. These surface states have a Dirac cone energy spectrum, which supports massless particles. Remarkably, the spin of surface Dirac electrons is locked perpendicular to the wave vector k in the 2D plane, leading to the suppression of electron scattering on impurities. Among the host materials for 3D TIs, wide strain HgTe films are considered some of the best, achieving a high mobility of 2D surface electrons $\mu \sim 100$ m^2 V^{-1} s^{-1} [12, 61–65].

Thermoelectric measurements provide valuable information about charge carrier sign and transport mechanisms in metals and semiconductors. The value of the thermoelectric coefficient is strongly influenced by the energy spectrum and time relaxation mechanism via the Mott relation.

In the previous section discussing 2D topological insulators, we mentioned that anomalously large thermopower has been predicted in this system based on the Mott relation [32]. A 2D TI features a pair of counterpropagating gapless edge modes inside the bulk gap with helical spin properties, proposed to be robust to backscattering [3–5, 11]. When the Fermi level approaches the conductance or valence band edge, the scattering rate of electrons in these helical one-dimensional modes is suggested to increase significantly due to 1D–2D scattering, leading to anomalous growth of the amplitude of the Seebeck signal and a change of its sign. However, this mechanism requires the complete suppression of scattering between edge states, which is not observed in realistic structures [11]. Experimental evidence has demonstrated that the observed thermopower is mostly due to the bulk contribution, while the resistance is determined by both edge and bulk transport [56].

In a 3D topological insulator, a comparable scenario is anticipated when the Fermi level intersects the boundary of the bulk bands. Figure 3b in Section 2 serves to exemplify this. Within the energy range indicated by the grey shading, the energy spectra of both the quasi-three dimensional holes and the topological surface electronic states overlap. Consequently, this spectrum results in additional 2D–3D scattering, which potentially enhances the thermoelectric power coefficients. Such mutual scattering has been directly detected in the resistance behavior [63, 64]. Recently, 2D electron–3D hole scattering has been deduced from nonmonotonic differential resistance of narrow 3D TI HgTe channels [66].

Another system, where the coexistence of the two distinct types of carriers with a different charge sign affects the transport properties, is a 2D semimetalic HgTe well of intermediate well width (~ 20 nm) [16, 67]. In this system, 2D electron–2D hole scattering directly results in temperature dependent resistivity ρ, which increases with temperature as $\rho \sim T^2$ in accordance with the prediction for electron-hole friction coefficient behavior [68]. We describe this situation in Section 6.

Thus, thermoelectric power is a very important tool to study the mechanism of scattering between carriers of different signs and even between carriers of different dimensions, as for example 1D–2D (2D topological insulators [32]) and 2D electron–2D holes (2D semimetals [69]).

5.2 Results

We measured the resistance and themopower in macroscopic samples by methods described in detail in the corresponding Section 3. Samples have the sandwich structure shown in 12a, and devices are macroscopic Hall bars, shown in Fig. 12b. Figure 12c, d displays the zero-magnetic-field resistances for two samples (marked as A and B) at different temperatures. The current I flows between contacts 1 and 6, while the voltage V is measured between the short-distance probes 2 and 3, and the resistance is calculated as $R = R_{1.6}^{2.3}$ (Figure 12b). The temperature-dependent behavior $R(V_g, T)$ reveals the diverse transport characteristics in distinct regions of the energy spectrum and has been previously examined in [63, 54]. Figure 3b indicates the specific characteristics of the energy spectrum of the strained HgTe layer, schematically reproduced in Fig. 12a. When the gate voltage shifts from negative to positive values, the electrochemical potential $\bar{\mu}$ moves from the conductance band ($\bar{\mu} > E_c$) through the bulk gap ($E_v < \bar{\mu} < E_c$) to the valence band ($\bar{\mu} < E_v$), as shown in Fig. 12c, d. The resistance in the bulk gap region stems from the helical surface electron states, with different densities in the top and bottom surfaces [63]. In the region $E_{DF} < \bar{\mu} < E_v$, two-dimensional surface electrons and 3D bulk holes coexist, and we observe a nonmonotonic temperature dependence of resistance: $R(T)$ increases below 15 K and decreases above 20 K. We attribute this behavior to 2D electron–3D hole scattering, similar to 2D electron–2D hole scattering in HgTe semimetal wells [67, 68]. In the region $\bar{\mu} < E_{DF}$, transport is dominated by 3D bulk holes, and we don't anticipate any peculiarities in resistance or thermopower behavior.

After determining the gate voltage and density interval with different transport properties, we investigated the thermoelectric response in our films. We measured the longitudinal thermovoltage $V_{xx} = S_{xx}\nabla T L$, where $L = 450$ μm is the distance between probes 1 and 6 along the temperature gradient ∇T (as shown in Fig. 12b). To examine the homogeneity of the temperature gradient, we also measured the longitudinal thermovoltage between probes 2–3 and 2–5, and found a reasonable proportionality to L.

Figure 13a, b displays the gate voltage dependences of the Seebeck coefficient S_{xx} at different temperatures in a zero magnetic field for two samples. One can see similar behaviours. The thermopower is negative in the region $E_v < \bar{\mu}$. As the gate voltage decreases towards the hole contribution, the Seebeck coefficient changes sign, crossing zero at the voltage corresponding to the transition from the electron-dominant to hole-dominant contribution. This transition is not coincident with the charge neutrality point, which was determined from the zero Hall resistance measurement in a magnetic field ([64, 65]), or with the positions of energies E_v or E_{DF}. The value of the Seebeck coefficient is larger for holes. Figure 13a, b shows the traces of S_{xx} versus V_g for different temperatures and for two samples. The temperature dependence of the Seebeck coefficient module is shown in Fig. 13c for selected gate voltages $V_g = 6$ and -6 V, corresponding to the electron- and hole-dominant regions. We found that S_{xx} grows linearly with temperature as $S_{xx} \sim T$ in the interval $10 < T < 25$ K.

In the region $E_{DF} < \bar{\mu} < E_v$, where 2D electrons and 3D bulk holes coexist, we are unable to distinguish the thermopower mechanism due to electron-hole scattering, which can modify the temperature dependence of $S_{xx}(T)$. A comparison between theory and experiment in this case requires a more

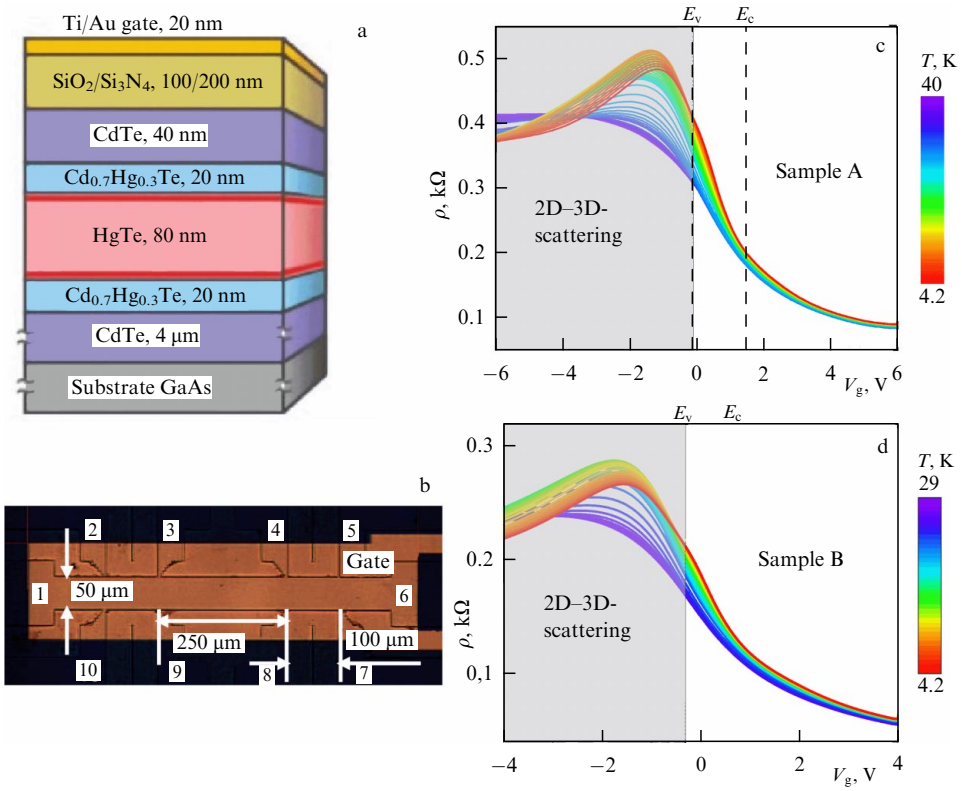

Figure 12. (a) Schematic of transistor. (b) Top view of sample. (c, d) Resistivity ρ as function of gate voltage measured for different temperatures for sample A (c) and B (d). Energy window where surface electrons and bulk holes coexist is marked by gray shading.

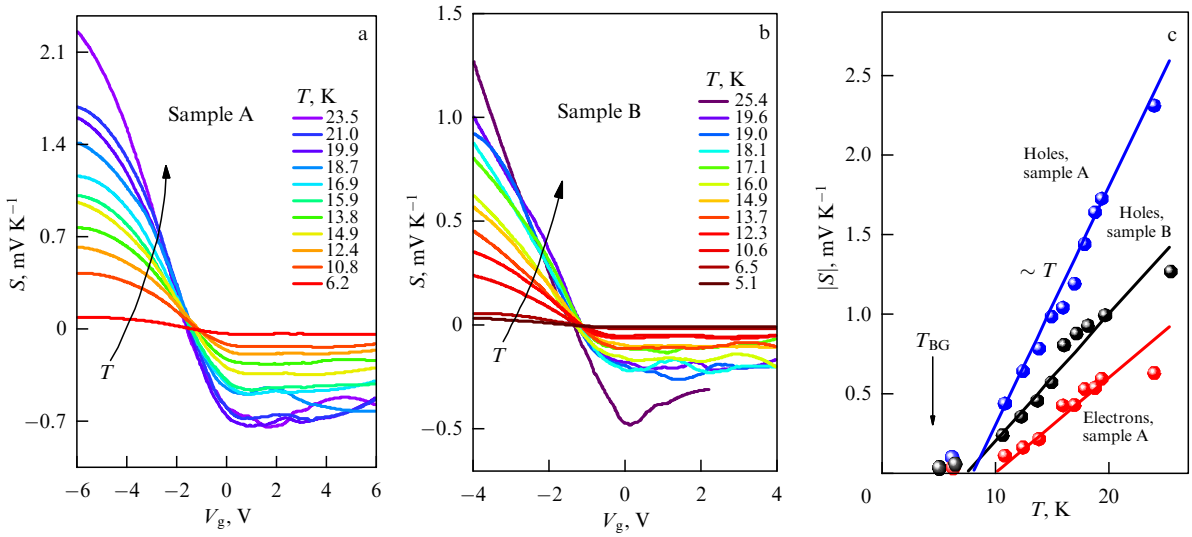

Figure 13. (a) Seebeck coefficient as function of gate voltage for different temperatures for samples A (a) and B (b). (c) Seebeck coefficient as function of gate voltage for different temperatures for sample B. (d) Temperature dependence of Seebeck coefficient for different voltages and samples: blue balls ($V_g = -6$ V, sample A), black balls ($V_g = 4$ V, sample B), red balls ($V_g = 6$ V, sample A). Solid lines correspond to $S_{xx} \sim T$. Arrows indicate Bloch–Gruneisen temperature.

advanced theory. We should note that previous research on 3D TIs did not reveal semimetallic behavior and features in the resistivity and thermopower due to electron-hole frictions, since the samples had lower mobility [70]. To further investigate the features observed in the resistance and thermopower measurements, we measured the derivative of resistance dR/dV_g, as shown in Fig. 14. The features in points E_c and E_v are clearly visible in both samples. Interestingly, these features coincide with a local minimum in the thermopower measurements.

Based on these observations, we attribute the local minima in the thermopower to the beginning of 2D–3D scattering. We expect this scattering to increase the absolute value of thermopower due to the differences in the thermoelectric properties of the 2D and 3D carriers. Further, we describe a more detailed analysis in order to fully understand the contribution of 2D–3D scattering to the thermopower in our samples.

In the region $\bar{\mu} < E_{DF}$, the transport is determined by 3D bulk holes, and we do not expect peculiarities in resistance and thermopower behavior.

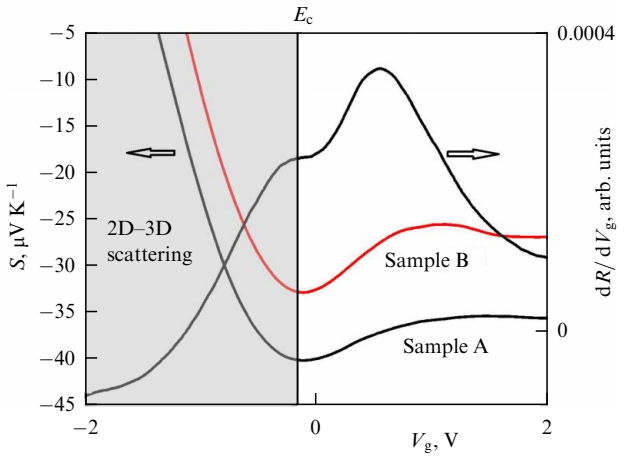

Figure 14. (a) Derivative of resistance $\mathrm{d}R/\mathrm{d}V_g$ as function of gate voltage at $T = 4.2$ K for sample B and Seebeck coefficient as function of gate voltage for samples A (black) and B (red). Energy window where surface electrons and bulk holes coexist is marked by gray shading.

5.3 Discussions

Detailed calculations of thermopower in 2D semimetals have been performed in papers [69, 71], where both contributions (diffusion and phonon drag) have been taken into account. The Seebeck coefficient in a zero magnetic field is given by

$$S_{xx} = \frac{\Lambda_x}{Z}\,, \tag{10}$$

$$Z = \left[m_e n_h \tau_h + m_h n_e \tau_e + (n_e - n_h)^2 \eta \tau_e \tau_h\right]^2, \tag{11}$$

$$\Lambda_x = \frac{1}{e}\left\{\left[A^e \tau_e m_h - A^h \tau_h m_e + (A^e + A^h)(n_e - n_h)\,\eta \tau_e \tau_h\right] \times \left[m_h \tau_e n_e + m_e \tau_h n_h + (n_e - n_h)^2 \eta \tau_e \tau_h\right]\right\}, \tag{12}$$

where $A^{e,h} = A^{e,h}_{dif} + A^{e,h}_{ph\text{–}dr}$ are the electron and hole terms corresponding to the diffusion and phonon-drag contributions to the Seebeck coefficient, respectively, n_e and n_h are the electron and hole densities, $m_e = 0.03m_0$ and $m_h = 0.3m_0$ are the electron and hole effective mass, $g_e = 1$ and $g_h = 2$ are the electron and hole valley degeneracy, τ_e and τ_h are the electron and hole transport scattering time, determined from the electron and hole mobilities, respectively, k is the Boltzmann constant, and $\eta = \Theta T^2$ is the electron-hole friction coefficient.

The diffusion contribution does not contain any adjustable parameters and is given by

$$A^{e,h}_{dif} = -\frac{\pi}{3\hbar^2}\, k^2 T m_{e,h}\, g_{e,h}\,. \tag{13}$$

The phonon drag contribution depends on the material specific phonon relaxation rate and the temperature regime. The system enters into the Bloch–Gruneisen (BG) regime at a very low temperature T when the acoustic phonon wave vector $q = 2k_F$, where k_F is the Fermi wave vector. In our HgTe system, we found that, for the densities $n_s \sim 10^{12}$ cm^{-2}, the characteristic temperature $T_{BG} = 2k_F s\hbar/k$ (s is the sound velocity) is around 4–6 K (Fig. 13d). If we propose that $\tau_{ph} = \text{const}$, then, for temperatures $T \gg T_{BG}$, we obtain

$$A^{e,h}_{ph\text{–}dr} = -\frac{1}{3\hbar^5}\, k \tau_{ph}\, m^2_{e,h}\, s p^2_{F_{e,h}} g_{e,h} B_{e,h}(q_T)\,, \tag{14}$$

where $q_T = kT/\hbar s$ is the thermal phonon wave vector, and, for acoustic phonons in cubic crystals, the function $B_{e,h}(q_T)$ reads

$$B_{e,h}(q_T) = \frac{\Lambda^2_{e,h} q_T}{2\delta s}\,, \tag{15}$$

where $\Lambda_{e,h}$ are the deformation potential constants, and δ is the crystal density. The data for the deformation potential $\Lambda_e = -4.8$ eV and $\Lambda_h = -0.92$ eV, for δ and s, we have $\delta = 8.2$ g cm^{-3}, $s = 3.2 \times 10^5$ cm s^{-1}. One can see that, in the temperature regime $T \gg T_{BG}$, both contributions $A^{e,h}_{dif}$ and $A^{e,h}_{ph\text{–}dr}$ linearly depend on temperature. Note that, in the monopolar limit in the regions $\bar{\mu} < E_{DF}$, where the transport is determined by 3D bulk holes, we obtain the following equations for diffusive and drag contributions (using subscript h):

$$S^{e,h}_{diff,\,ph\text{–}dr} = \pm \frac{A^{e,h}_{dif,\,ph\text{–}dr}}{e n_{e,h}}\,. \tag{16}$$

In the conduction band, where $\bar{\mu} > E_c$, bulk and surface carriers coexist. However, for simplicity, we assume that they are described by a single density n_e, and use Eqn (16) (subscript n) to calculate the Seebeck coefficient. Since the HgTe layer is not thick, we can consider the bulk carriers a quasi-two-dimensional system. Figure 15(a) shows a comparison of the theoretical Seebeck coefficients calculated using equations (10)–(16) for different values of the parameter Θ and the experimental curve measured at $T = 10.8$ K as a function of V_g. The parameter Θ is related to the electron-hole friction coefficient η and is responsible for the features of the thermoelectromotive force in the region $E_{DF} < \bar{\mu} < E_c$, where surface electrons and bulk holes coexist. Figure 15(b) shows a comparison of the theoretical Seebeck coefficients calculated using equations (10)–(16) for different temperatures as a function of V_g. Good quantitative and qualitative agreement with the theory is observed.

To calculate the diffusion and phonon drag contributions to the monopolar regions, we use equations (13)–(16) for the sample parameters determined from conductivity measurements. We do not use any adjustable parameters in our calculations of the diffusive thermo e.m.f. For the phonon drag contribution, we assume a constant phonon relaxation time $\tau_{ph} = 0.6 \times 10^{-7}$ s, which corresponds to a relaxation length $l_{ph} = s\tau_{ph} = 0.2$ mm, close to the sample size. We argue that the phonon relaxation length is determined by phonon scattering on the substrate boundaries. Since we found that $S^{e,h}_{diff} \ll S^{e,h}_{ph\text{–}dr}$, we conclude that the phonon drag contribution dominates at high temperatures $T > 4.2$ K. We also note that the temperature dependence of the Seebeck coefficient is linear for temperatures above T_{BG} for both contributions.

In the bipolar region $E_{DF} < \bar{\mu} < E_c$, where both surface electrons and bulk holes coexist, we calculated the thermopower using Eqns (10)–(15). However, our simplified model assumed a constant electron-hole friction coefficient η that does not depend on the electron and hole densities. This model is too simplistic to adequately describe the shape of the thermopower behavior in this region. Figure 15a demonstrates that the shape of the curve $S(V_g)$ is closer to the experimental one for a smaller $\Theta = 1.0 \times 10^{-38}$ J s K^{-2}, which is smaller than the friction coefficient for a 2D electron and 2D hole system, $\Theta = 4.8 \times 10^{-38}$ J s K^{-2} [68]. The inset

shows the Seebeck coefficient zoomed in on the voltage interval $E_v < \bar{\mu} < E_c$ for $T = 4.2$ K. We observe that the thermopower is enhanced near the point $\bar{\mu} \simeq E_v$, which we attribute to the 2D Dirac electron-3D bulk hole scattering. However, the feature near E_v is smeared out at higher temperatures.

It is important to note that the equations in the monopolar regime (16) cannot be obtained from Eqn (11), (12) by transitioning to the monopolar case, because they are derived under the assumption that the Fermi gases are degenerate. The transition to the monopolar limit at low temperatures occurs in a relatively narrow range of the chemical potential $\Delta\bar{\mu} \sim T$ (see Fig. 15b), which may lead to discontinuity in the calculated thermopower around transition points. While our experiment offers an interesting outlook on thermopower in this region, more experimental and theoretical work is required to understand the behavior of the friction between 2D electrons and 3D holes in a 3D topological insulator.

We conducted a comparison between experiments and the monopolar model (Eqn (16)), which only considers independent contributions from 2D electrons and 3D holes to thermopower (not shown here). However, we found significant disagreement between the theory and experiments, further supporting the presence of mutual electron-hole friction in our system, as reported in previous studies [12, 63, 66].

In Figure 15b, we present the temperature dependence of the theoretical curves $S(V_g)$. As expected, in the monopolar region, $S(V_g)$ is proportional to temperature, in agreement with experimental observations (Fig. 13c). On the other hand, in the bipolar region $E_{DF} < \bar{\mu} < E_c$, the Seebeck coefficient $S(V_g)$ grows faster with temperature due to the mutual friction coefficient η having a temperature dependence of $\eta = \Theta \times T^2$. It should be noted that the model is valid only for degenerate Fermi gases and cannot be applied at high temperatures near the charge neutrality points. Therefore, a more advanced theoretical approach is required to accurately describe this behavior, which is beyond the scope of our experimental study.

5.4 Conclusions

In summary, we present a comprehensive study of the thermoelectric properties of a three-dimensional topological insulator based on an HgTe film. The experimental results are compared with a theoretical model, and the behavior of the thermoelectric coefficients is analyzed in both the monopolar and bipolar regimes. In the monopolar regimes, we show that the drag contribution dominates over diffusion thermopower, and we determine the phonon relaxation length by taking this contribution into account. The results reveal that phonon scattering at the structure boundaries plays a significant role, and the phonon relaxation length is temperature independent. In the bipolar region, we observe modification of the Seebeck coefficient due to 2D electron–3D hole scattering, and the theoretical analysis shows good agreement with the experimental data. However, a more detailed understanding of the mutual friction behavior is necessary to fully comprehend the thermopower in this nontrivial regime. Overall, this work sheds light on the fundamental thermoelectric properties of topological insulators and provides valuable insights for the development of future thermoelectric devices.

6. Thermopower in two-dimensional semimetal in HgTe quantum well

The coexistence of two distinct carrier types of opposite sign in a 2D semimetal in an HgTe QW creates quite an interesting situation as regards the effect of their interaction on various transport phenomena. In particular, one would expect the effect of binary collisions between different type of quasiparticles. According to the Pauli exclusion principle, only carriers in the energy interval of the order of kT around the Fermi energy may participate in such collisions, which would supposedly result in a $\sim T^2$ scaling of resistivity. The resistance of a single component system is unaffected by the binary collisions, unless Umclapp processes, involving the presence of the reciprocal lattice vector in the momentum

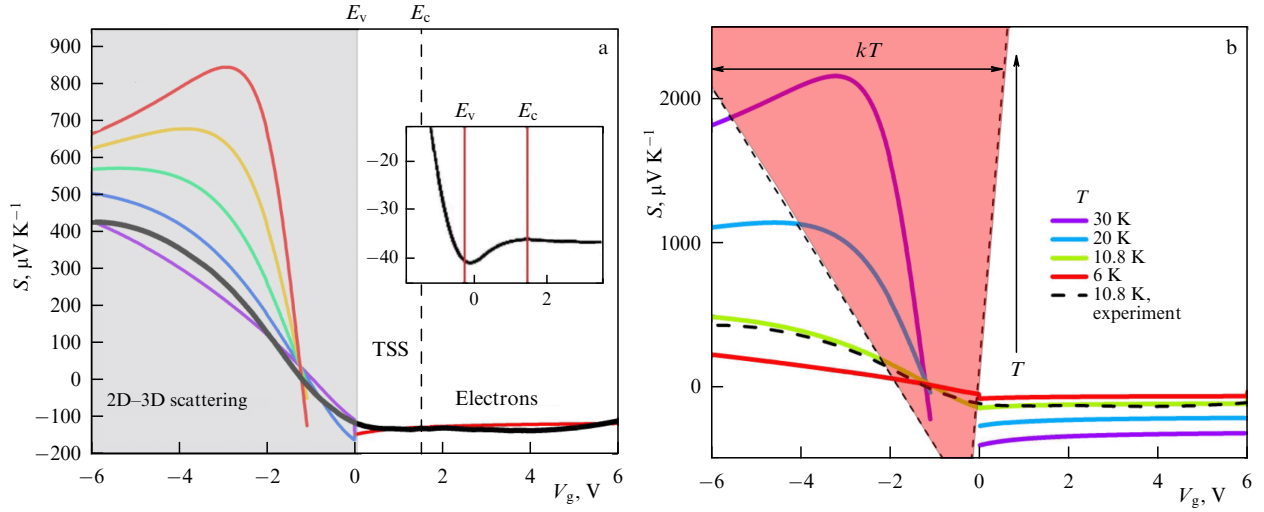

Figure 15. (a) The Seebeck coefficient as a function of the gate voltage calculated from Eqns (10)–(16) with the parameters given in the text and for different values of Θ: 0.1; 0.25; 0.5; 1; 2 ($\times 4.8 \times 10^{-38}$ J s K^{-2}). The black curve is the Seebeck coefficient measured at $T = 10.8$ K. The range of V_g, in which surface electrons and bulk holes coexist, is marked with a gray background. The inset shows the experimental dependence of the Seebeck coefficient at $T = 4.2$ K in the range $E_v < \mu < E_c$, where topological surface states (TSS) dominate the transport. (b) The Seebeck coefficient as a function of gate voltage calculated from Eqns (10)–(16) with the parameters given in the text and for various temperatures. The energy range $\mu \sim kT$, in which the concept of degenerate electrons and holes no longer holds, is marked with a red background. Equations (10)–(16) cannot be applied to this region. The dotted curve corresponds to the Seebeck coefficient measured at 10.8 K.

conservation equation, are allowed. This is due to the fact that, in a single component system, all carriers have the same effective mass, and the momentum conservation automatically implies the conservation of the total current. However, if carriers of more than one type are present in the system, the momentum conservation in the acts of binary scattering involving particles of different types no longer ensures conservation of electrical current. In this case, the resistance should become sensitive to binary collisions between different types of particles [72–77].

The expected experimental evidence of such sensitivity is the $\sim T^2$ scaling of resistivity, observed for the first time in a 2D semimetal (electron-hole system) on the basis of an HgTe quantum well and successfully described by a theory [67, 68] where the binary collisions were included in the form of an interparticle friction coefficient proportional to T^2 (Fig. 16a). Numerous theoretical papers have examined the thermoelectric properties of semimetals, with a particular focus on the effect of inelastic electron-hole scattering on deviations from the Wiedemann–Franz law [78–80]. Recent research has revealed that electron-hole scattering has a significant impact on thermopower, resulting in a critical suppression of the Lorenz ratio.

The thermopower in a 2D electron-hole system in an HgTe quantum well has been experimentally investigated [69]. A corresponding theory has been developed that takes into account the interparticle scattering playing an important role in the two principal contributions to thermopower. A comparison between theory and experiment has revealed that the thermo e.m.f. in a 2D electron-hole system is determined by two contributions: the diffusion and the phonon drag, with the latter mechanism of thermopower prevailing over the first one. Conclusions have been drawn about the important role of electron-hole scattering in the formation of both thermoelectric power mechanisms.

6.1 Resistance and mobility in 2D semimetals

The transport and thermoelectric measurements discussed in this section were performed using macroscopic types of samples with a quantum well width of 21 nm and the methods described in detail in the corresponding Section 3.

Figure 16a shows the typical dependence of a 2D semimetal resistance on gate voltage and temperature. At $V_g \approx -0.6$ V, there is a transition between a two-dimensional metal and two-dimensional semimetal accompanied by a sharp change in the character of the temperature dependence of the resistance. To the right of the transition, the $\rho(T)$ is weak and represents a typical temperature dependence of a two-dimensional metal at $k_F l \gg 1$ (k_F and l are the wave vector and mean free path of the electron) and low temperatures when the phonon scattering is almost absent and the temperature dependence is determined by weak-localization effects. A noticeable change in $\rho(T)$ is observed to the left of the transition to the semimetal state. Here, $\rho(T)$ is due to electron-hole scattering and is thereby proportional to the temperature squared (Fig. 16b).

The gate voltage dependence of such parameters as electron density $n_e(V_g)$, hole density $n_h(V_g)$, electron mobil-

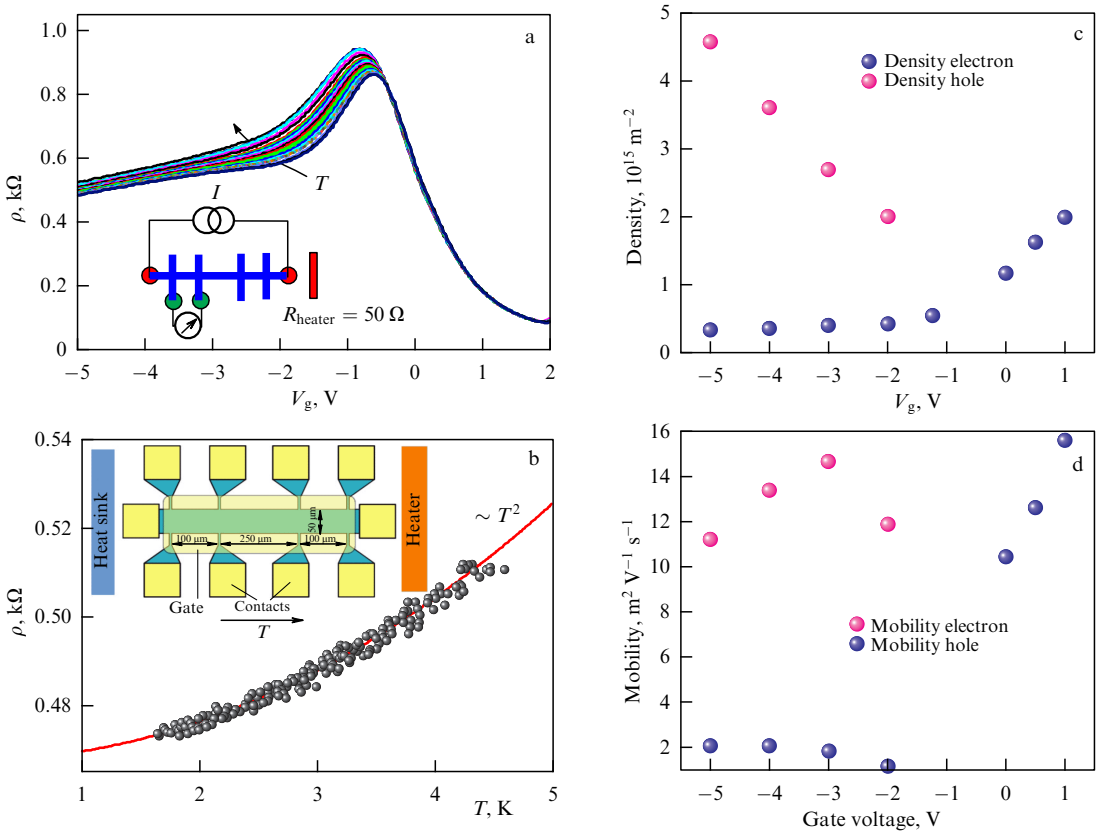

Figure 16. (a) Resistance versus gate voltage at various temperatures in range $T = 2.1-6$ K. (b) Temperature dependence of resistance at $V_g = -5$ V. Inset shows structure under study and direction of temperature gradient created by heater (on right) and heat sink (on left). (c) Electron and hole density and (d) electron and hole mobility versus gate voltage. Parameters determined by fitting two-component Drude model to low field classical magnetoresistance dependences of $\rho_{xx}(B)$ and $\rho_{xy}(B)$.

ity $\mu_e(V_g)$, and hole mobility $\mu_h(V_g)$ can be determined from fitting the two-component Drude model to low field classical magnetoresistance dependences of $\rho_{xx}(B)$ and $\rho_{xy}(B)$. $\Theta(V_g)$ — the coefficient characterizing the strength of the electron-hole friction is found by fitting the experimental $R(T)$ dependence in the region of the band overlap to the theoretical model that takes into account the friction between holes and electrons [67, 68].

The parameters thus found are summarized in Fig. 16c, d, from which the following conclusions can be made: (1) the semimetallic state begins at $V_g \approx -1$ V, (2) at the charge neutrality point, $P_s = N_s \approx 10^{11}$ cm^{-2}, (3) the conduction and valence band overlap region is about 10 meV, in agreement with earlier studies of HgTe 20 nm QWs [16, 67], (4) for all negative biases in Fig. 16a, the Fermi level never completely leaves the conduction band, being pinned there by a very high hole density of states in the valence band.

6.2 Thermopower in two-dimensional semimetal

Figure 17a shows the gate voltage dependences of the temperature-gradient-induced potential difference V_{th} between the potentiometric contacts of the bar with length $L = 100$ μm. The inset of this figure shows the dependence of the thermopower signal on the power applied to the heater. It is clearly seen that the measured signal is proportional to this power, which indirectly indicates that the measured signal is indeed due to the thermopower rather than possible pickups. We now qualitatively analyze the behavior of the thermopower shown in Fig. 17a. We begin with the dependence on the gate voltage. At gate voltages corresponding to the electron metal, the thermopower is relatively low and decreases with an increase in the density according to the Mott formula for the thermopower of metals. The thermopower changes sign near the transition point and begins to increase almost linearly with the development of the semimetal state (with an increase in the density of holes). Figure 17b shows the gate voltage dependences of the Seebeck coefficient $S = V_{th}/\Delta T$ (ΔT is the temperature difference between potential contacts on which the V_{th} signal is measured) at different temperatures. It is seen that the Seebeck coefficient increases with the temperature of the sample.

To more accurately describe the experimental results obtained in this work, we developed a theory of the diffusion component of the thermopower for a two-dimensional electron-hole system consisting of two types of degenerate particles, electrons and holes. In the presence of the temperature gradient, chemical potential, and electron-hole friction, the average velocities in the subsystems satisfy the equation

$$n_v e_v \mathbf{E} - g_v m_v \frac{\pi T}{3\hbar^2} \nabla T - \frac{m_v n_v}{\tau_v} \mathbf{V}_v = \eta n_v n_{\bar{v}} (\mathbf{V}_v - \mathbf{V}_{\bar{v}}) . \quad (17)$$

Here, the subscript $v = (e, h)$ specifies quantities referring to electrons (e) and holes (h); n_e (n_h) is the density of electrons (holes); g_v is the number of valleys ($g_e = 1, g_h = 2$); $\mathbf{V}_v, m_v, e_v$ are the average velocity, effective mass, and charge of particles of type v ($e_{e,h} = \mp e$, e is the charge of the hole), respectively; τ_v is the relaxation transport time on impurities; η is the friction coefficient; and T is the temperature in energy units. The friction coefficient $\eta = \Theta T^2$ is determined by electron-hole scattering through the Landau mechanism.

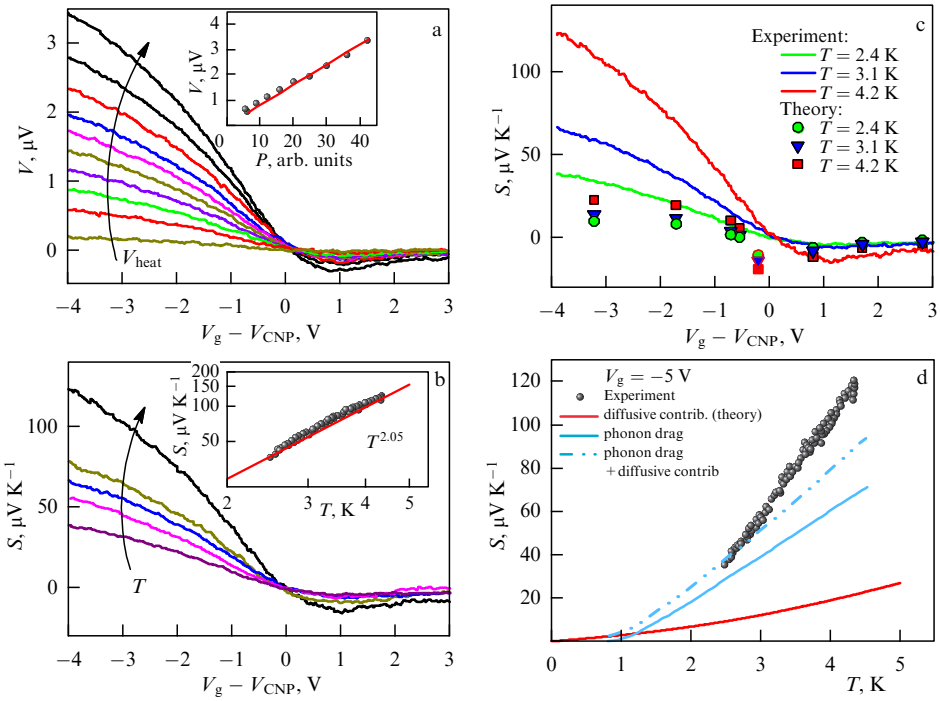

Figure 17. (a) Thermopower versus gate voltage for heater voltages V_{Heat} increasing (as shown by arrow) from 2 to 6.5 V with step of 0.5 V, at temperature $T = 4.2$ K. Inset shows thermopower versus heater power at $V_g = -5$ V. (b) Seebeck coefficient versus gate voltage for temperatures $T = 2.4$; 2.8; 3.1; 3.3; and 4.2 K. $V_{CNP} = -1.1$ V. (c) Seebeck coefficient versus gate voltage at temperatures, $T = 2.4$; 3.1; 4.2 K according to (lines) experiments and (balls) calculations by Eqns (18) and (19) to left and right of charge neutrality point, respectively, with parameters obtained from transport measurements. (d) Temperature dependence of Seebeck coefficient in two-dimensional semimetal: (balls) experiment for $V_g = -5$ V; lower red line is diffusion contribution that corresponds to indicated gate voltage and calculated by Eqn (18); (solid blue line) represents calculated phonon drag contribution as explained in text; dashed blue line is sum of phonon drag shown by solid blue line and diffusion contribution shown by red line.

Equation (17) is a generalization of equations presented in [68, 81] to the case of the existence of a temperature gradient.

From the condition that the total current density $\mathbf{j} = e(-n_e\mathbf{V}_e + n_h\mathbf{V}_h)$ vanishes, the Seebeck coefficient is obtained in the form

$$S = -\frac{\pi}{3e\hbar^2}T \times \frac{m_e m_h(g_e\tau_e - g_h\tau_h) + \eta\tau_e\tau_h(g_e m_e + g_h m_h)(n_e - n_h)}{m_h n_e\tau_e + m_e n_h\tau_h + (n_e - n_h)^2\eta\tau_e\tau_h}. \quad (18)$$

It is noteworthy that the contribution to the current from any type of charge carrier in Eqn (18) is nonzero even at zero carrier density; i.e., this formula does not have any monopolar limit:

$$S^{(0)}_{e,h} = \mp\frac{\pi}{3e\hbar^2}T\frac{m_{e,h}\,g_{e,h}}{n_{e,h}}. \quad (19)$$

In contrast to Eqn (18), there are no terms corresponding to the second type of carriers, in particular, its relaxation time and friction. The reason formulas (18) and (19) are different is because they are obtained under the assumption that Fermi gases are degenerate. Indeed, the transition to the monopolar case at low temperatures occurs in a relatively narrow range of the chemical potential $\Delta\mu \sim T$. The friction between different types of carriers distorts the linear temperature dependence of S. In the low-temperature limit, $\eta \propto T^2$, which leads to third-order temperature corrections to the linear dependence.

The friction can become a prevailing mechanism of scattering ($\eta \to \infty$) at higher temperatures. In this case, Eqn (18) becomes independent of all relaxation constants:

$$S = -\frac{\pi}{3e\hbar^2}T\frac{m_e g_e + m_h g_h}{(n_e - n_h)}. \quad (20)$$

This formula is valid far from the CNP. The Seebeck coefficient S changes sign near this point (more precisely, at the point where the numerator of Eqn (18) changes sign). The Seebeck coefficient in the region of applicability of Eqn (20) also has a linear temperature dependence similar to that at low temperatures but with a larger slope. As a result, the dependence can be close to a quadratic law in the intermediate temperature range.

Figure 17c shows the Seebeck coefficients $S(V_g)$ calculated by Eqns (18) and (19) in comparison with experimental data. All parameters necessary for the calculation by Eqns (18) and (20) (mobilities and densities of electrons and holes and the friction coefficient) and their dependence on the gate voltage were obtained previously from transport measurements [68] and from the cyclotron resonance (effective masses of electrons and holes) [63]. The temperature gradient necessary for the determination of the Seebeck coefficient was measured experimentally according to the method described at the beginning of this paper. Thus, the comparison of the theory and experiment in Fig. 17c is free of fitting parameters.

The qualitative behavior of the Seebeck coefficient to the right of the charge neutrality point, where the electron metal exists, corresponds to the Mott theory for metals, which predicts a decrease in the Seebeck coefficient with an increase in the carrier density. For comparison with experimental data in this range of gate voltages, we used the monopolar formula (19) for electrons, which is the Mott formula under the assumption that $\tau(\varepsilon) = \text{const}$ (τ is the pulse relaxation time and ε is the energy). As is seen, the Seebeck coefficients calculated by Eqn (19) are in satisfactory agreement with experimental points (Fig. 17c).

On the contrary, to the left of the charge neutrality point in Fig. 17c, i.e., in the region of gate voltages corresponding to the formation of the two-dimensional semimetal, agreement between experiment and theory (Eqn (18)) is much worse. In this range of gate voltages, the theory gives Seebeck coefficients about one-fourth those of experimental values (see Fig. 17c). This discrepancy apparently appears because Eqn (18) describes only the diffusion contribution to the thermopower of the semimetal. However, the measured thermopower can include not only the diffusion contribution but also the phonon drag contribution [82], which is disregarded in our theory. As is known, the phonon drag is proportional to the mass squared of charge carriers. The masses of electrons and holes in the 20-nm HgTe quantum well are $m_e = 0.025m_0$ and $m_h = 0.15m_0$, respectively. For this reason, the phonon drag contribution on the left of the charge neutrality point (i.e., in the region where holes dominate) is significant, whereas this contribution on the right of the charge neutrality point, where the two-dimensional metal exists, is negligible.

Figure 17d shows the experimental points for the temperature dependence of the Seebeck coefficient at $V_g = -5$ V when the holes predominate. The experimental dependence $S(T)$ is linear and extrapolates to $S = 0$ at $T_0 \approx 1.5$ K. We compare this data with the theoretical formulae for different assumptions [83]. Theoretical curves in Fig. 17d correspond to the calculated diffusion and phonon drag contributions to S_{xx}, respectively. We use the following values of parameters at $V_g = -5$ V: $n_e = 3.3 \times 10^{10}$ cm^{-2}, $n_h = 4.57 \times 10^{11}$ cm^{-2}, $m_e = 0.025m_0$, $m_h = 0.15m_0$, $\mu_e = 11.2\,\text{m}^2\ \text{V}^{-1}\ \text{s}^{-1}$, $\mu_h = 2.1\,\text{m}^2\ \text{V}^{-1}\ \text{s}^{-1}$, $\Theta = 4.8 \times 10^{-38}\ \text{J s K}^{-2}$. The phonon drag contribution was found for the phonon relaxation mechanism with a constant mean free path. We used the literature data for the deformation potential: $\Lambda_e = -4.6$ eV [84] and $\Lambda_h = -0.92$ eV [85]; for the HgTe density and sound velocity, we have $\rho = 8.2$ g cm^{-3}, $s = 3.2 \times 10^5$ cm s^{-1}. According to Fig. 17d, the experimental behavior contradicts the diffusion contribution, which is not linear. The diffusion contribution value is smaller than the one in the experiment. Moreover, the temperature dependence substantially differs from the experimental one: a gradually growing slope in the theory, instead of a linear experimental dependence, extrapolating to 0 at $T = 1.5$ K. In calculating the phonon drag contribution, we ignored the Herring phonon relaxation mechanism: this one yields too large a value, exceeding by many orders the experimental data. In addition, it has too strong (and inverse, compared with the experiment) a temperature dependence. Therefore, we calculated the phonon drag contribution for a constant mean free path of phonons. The phonon drag for a constant mean free path of phonons gives a result most in agreement with the experimental curve. The coefficient η weakly influences the dependence and can be disregarded. To produce a large enough drag contribution, the phonon mean free path l_{ph} should also be large. However, it is limited from above by the sample size of ~ 0.1 cm. The other stronger limitation by a transversal sample width of $\sim 10^{-5}$ cm is not pertinent, because phonons can penetrate beyond the

metallic gate. Thus, the permitted domain of l_{ph} is 10^{-5} cm $< l_{ph} < 0.1$ cm. The satisfactory fitting to the experimental curve is reached for $l_{ph} = 0.06$ cm. This value gets into the admissible range. One can see that the linear dependence on the temperature at a relatively high temperature is replaced by the strong power-like behavior at a low temperature. This corresponds to the experimental finding. Hence, we should conclude that the drag prevails, but the temperature dependence is linear, because the mean free path is limited. The ballistic phonon drag, which has a nonlinear temperature dependence, fits the experiment worse.

6.3 Conclusion

In conclusion, the behavior of the thermo e.m.f. of a two-dimensional semimetal in an HgTe quantum well has been studied in a zero magnetic field. Experimental gate voltage dependences of the thermo e.m.f. were analyzed at different temperatures. The obtained experimental dependences were compared with the theory, in which the behavior of the corresponding transport coefficients is explained taking into account the mutual friction of two groups of carriers of opposite sign, present in the quantum well. It is shown that the calculated values of the transport coefficients corresponding to the diffusion contribution are approximately an order of magnitude smaller than those obtained in the experiment. Thus, the thermo e.m.f. of the two-dimensional semimetal in the HgTe quantum well is determined mainly by the contribution from the phonon drag. Taking this contribution into account makes it possible to determine the phonon relaxation length, which turns out to be temperature independent and caused by phonon scattering at the structure boundaries.

7. Thermopower in 2D Weyl semimetal

7.1 Introduction

Recent theoretical and experimental studies suggest that 6.3-nm HgTe quantum wells can host a two-dimensional Weyl semimetal, which is a topological phase of matter that exhibits Weyl fermions as its elementary excitations. A two-dimensional Weyl semimetal is a type of material that exhibits a nontrivial electronic band structure in two dimensions, leading to the emergence of Weyl points in the Brillouin zone. Weyl points are those in the momentum space where the valence and conduction bands touch each other, leading to a nonzero Berry curvature and topologically protected surface states.

In contrast to three-dimensional Weyl semimetals, two-dimensional Weyl semimetals do not have a bulk bandgap. Instead, they have a topologically nontrivial band structure with a Dirac-like dispersion relation near the Weyl points.

We present an experimental study of the transport properties of a gapless HgTe quantum well with a thickness of 6.3–6.5 nm. Figure 18a shows a schematic of the energy spectrum of this system. The well energy exhibits a single valley cone in the energy spectrum, describing unusual electron transport properties [12, 18, 63, 86]. However, the valence band also contains a local valley formed by heavy holes, in addition to the Dirac-like holes in the center of the Brillouin zone. The energy minimum of heavy holes is marked by E_v. The coexistence of 2D electrons and holes has been observed previously in single wide HgTe-based quantum wells in the semimetallic regime, with the spectrum modification depending on the well thickness [12]. As we discussed in Section 2 at the critical thickness d_c, equal to 6.3–6.5 nm, the band gap collapses, and a second region begins where a 2D topological insulator with an inverted energy spectrum exists, with a third region emerging for $d > 12$ nm, where local valleys with heavy holes overlapping electrons in the conduction band create a 2D semimetal state [67, 68]. Even thicker films of strained HgTe ($d \sim 50-60$ nm) have been identified as three-dimensional topological insulators and studied [61, 64, 71]. The evolution of the spectrum is shown in the Fig. 1 in Section 2.

The coexistence of 2D electrons and holes in HgTe semimetals leads to a number of unusual properties, including a quadratic temperature dependence of the resistivity at low temperatures due to electron-hole scattering [67, 68]. This effect is a result of the momentum-conserving normal interparticle scattering, which has a negligible effect on the resistivity in the absence of the Umklapp process. In three-dimensional topological insulators, the overlap between a 2D topological surface state and 3D bulk holes leads to an unusual temperature dependence of the resistivity due to electron-hole scattering [56, 64]. The coexistence of Dirac-like holes and heavy holes at finite wave vector k leads to an increase in the resistance with temperature, as the low-mobility heavy holes absorb momentum during a collision [68]. Thus, the gapless HgTe well offers a new platform to study the scattering between conventional and Dirac particles.

The thermoelectric properties of materials are very sensitive to the scattering mechanism and can be used to obtain complementary information on intercarrier collisions. Previous studies of resistivity and thermoelectric transport properties in HgTe semimetals [56, 67] and 3D HgTe films [71], described in the previous sections, have extracted carrier-carrier scattering parameters.

Moreover, unlike previous systems, Weyl semimetals have a linear spectrum and are expected to exhibit an enhancement in the Seebeck coefficient due to the energy dependence of the density of states. The Bethe–Sommerfeld expansion for the Seebeck coefficient can be expressed as

$$S = \frac{\pi^2}{3}\frac{k_B}{e}(k_B T)\left[\frac{1}{D_\varepsilon(\varepsilon)}\frac{dD_\varepsilon(\varepsilon)}{d\varepsilon} + \frac{1}{\tau(\varepsilon)}\frac{d\tau(\varepsilon)}{d\varepsilon}\right], \qquad (21)$$

where D_ε is the density of states, τ is the relaxation time, and both are energy dependent. Therefore, the Seebek coefficient depends on the terms related to the density of states and mobility.

Graphene is a well-known example of a material with a Dirac spectrum. The thermoelectric response in materials can arise from two mechanisms: diffusion-driven and phonon drag. Due to weak electron-phonon coupling in graphene, the phonon drag contribution to the thermoelectric response is assumed to be negligible, and the diffusion mechanism dominates at low temperatures. Several studies have analyzed the thermopower of graphene within the temperature range of 10–300 K, including those in paper [87].

7.2 Experimental results and discussion

The resistivity $\rho(V_g)$ in a zero magnetic field for five samples, each fabricated from different wafers and at different times, is depicted in Fig. 18b. Typical parameters of the devices, including the well width d, gate voltage V_{CNP} at the Dirac

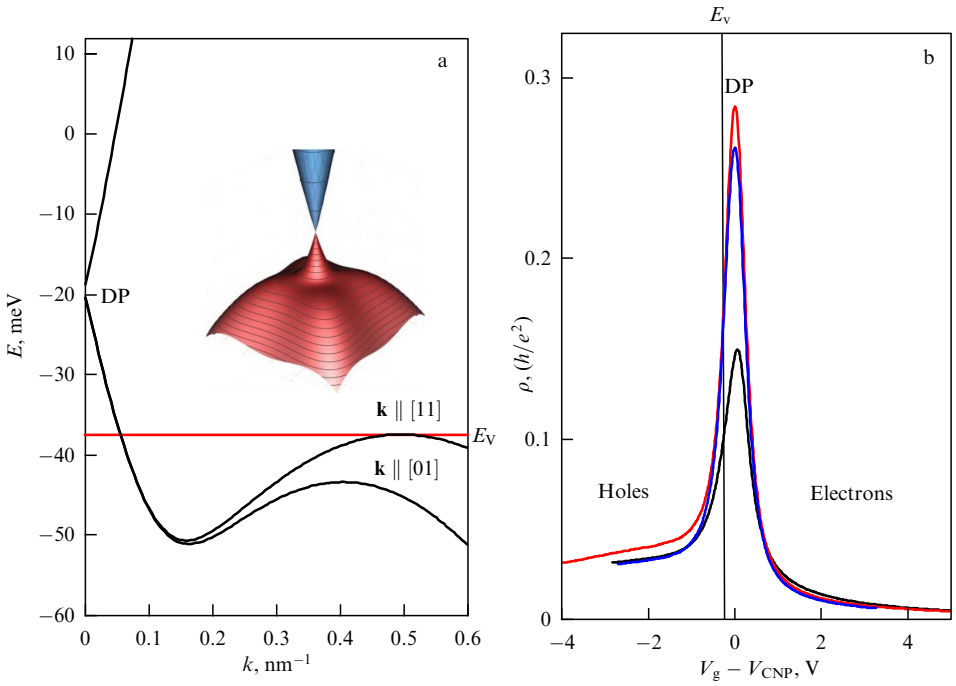

Figure 18. Schematic of energy spectrum of 6.3-nm-wide HgTe quantum well. (b) Resistance as function of gate voltage for different samples, $T = 4.2$ K. Red line — sample A, blue line — sample B, black line — sample C.

Table 2. Some typical parameters of electron system in gapless HgTe quantum well at $T = 4.2$ K.

Sample	d, nm	V_{CNP}, V	ρ_{max} (h/e^2)	μ, cm^2 V^{-1} s^{-1}
A	6.3	−1.8	0.28	56,000
B	6.4	−1.28	0.27	90,000
C	6.3	−1.16	0.15	59,600

point position, resistivity value ρ_{max} at the CNP, and electron mobility $\mu = \sigma/n_s e$ for density $n_s = 10^{11}$ cm^{-2}, are listed in Table 2.

When the chemical potential crosses from the electron to the hole side of the spectrum, the resistivity exhibits a narrow peak. Near the Dirac point (DP), it is expected that the resistivity value is close to the universal value $h/2.5e^2$ predicted for transport in this system in terms of percolation through a network of one-dimensional conducting channels [21, 88, 89]. For the electron side at higher electron densities, the electron energy spectrum becomes linear, and the pulse relaxation time and conductivity can be calculated from equations (1) and (2), leading to a conductivity $\sigma(n_s)$ that is nearly linear with electron density. However, fluctuations in the gap due to roughness may lead to additional scattering far from the charge neutrality point. This nontrivial mechanism of scattering is considered in [90]. The behavior of conductivity on the hole side is complex due to the nonmonotonic dependence of the Fermi energy. In a two-dimensional system, the behavior of the Fermi level is strongly influenced by the density of states. In a conventional 2D electron gas, the Fermi level is directly proportional to the charge concentration, since the density of states remains constant. However, in a system with a linear Dirac-like spectrum, the Fermi level (ε_F) is proportional to the square root of the charge density. When the chemical potential approaches energy $E_v \sim 15-20$ meV, it gets trapped by the heavy holes and its dependence on density becomes almost negligible.

The density of states for a particle with a linear spectrum is directly proportional to its energy. However, in order to address any peculiarities at the DP, we incorporated a Gaussian distribution to smooth out any potential inhomogeneities that may have been present. Finally the density of states is given by

$$D_\varepsilon(\varepsilon) = \frac{\varepsilon}{2\pi\hbar v_F^2}\left(\mathrm{erf}\left(\frac{\varepsilon}{\sqrt{2}\varsigma}\right) + 1 - \mathrm{erf}\left(\frac{\varepsilon}{\sqrt{2}\varsigma}\right) + \sqrt{\frac{2}{\pi}}\frac{2}{\varepsilon}\varsigma\exp\left(-\frac{\varepsilon^2}{\varsigma^2}\right)\right). \quad (22)$$

The density of states for heavy holes remains constant across different energy levels, but it is affected by disorder. As a result of the disorder, the density of states for heavy holes near the valence band edge becomes broadened, which is quantified by the parameter δ. Note that, due to the heavy mass value of heavy holes, their density of states is almost ten times larger than that of Dirac charge carriers. The conductivity of the Dirac particle is given by Eqn (1), while the conductivity and mobility of the heavy holes may be obtained from the conventional transport equations.

Using the experimentally determined total conductivity, we can distinguish between the conductivity of Dirac particles and heavy holes by applying Eqn (1) and Eqn (22). The outcomes of this separation are presented in Fig. 19a. We calculated the relaxation time for electrons and holes separately and plotted the results in Fig. 19b. The figure shows the relaxation time for each carrier type, providing insight into their behavior with the chemical potential variation. A nonmonotonic dependence with energy ($\bar{\mu}$) can be seen, which indeed can affect the Seebeck coefficient in accordance with Eqn (21).

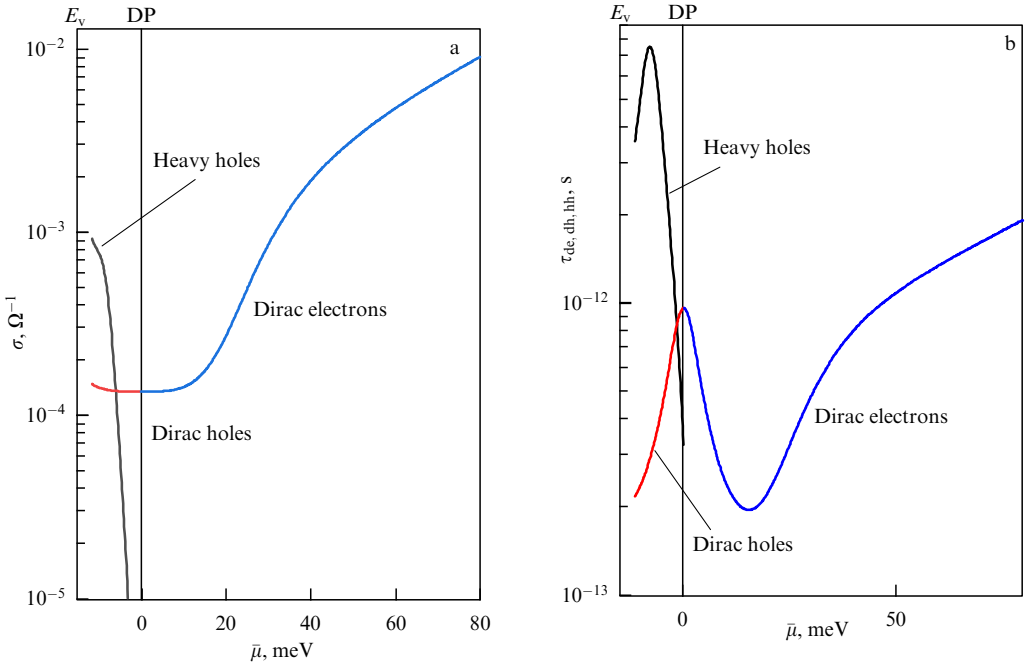

Figure 19. (a) Conductivity of different subbands in gapless 6.3-nm HgTe quantum well as function of chemical potential for sample A. (b) Transport relaxation time extracted from conductivity and energy dependent density of states. Parameters for density of states are $\delta = 5$ meV, $\varsigma = 3$ meV (22). Blue line — Dirac-like electrons, red line — Dirac-like holes, black line — heavy holes.

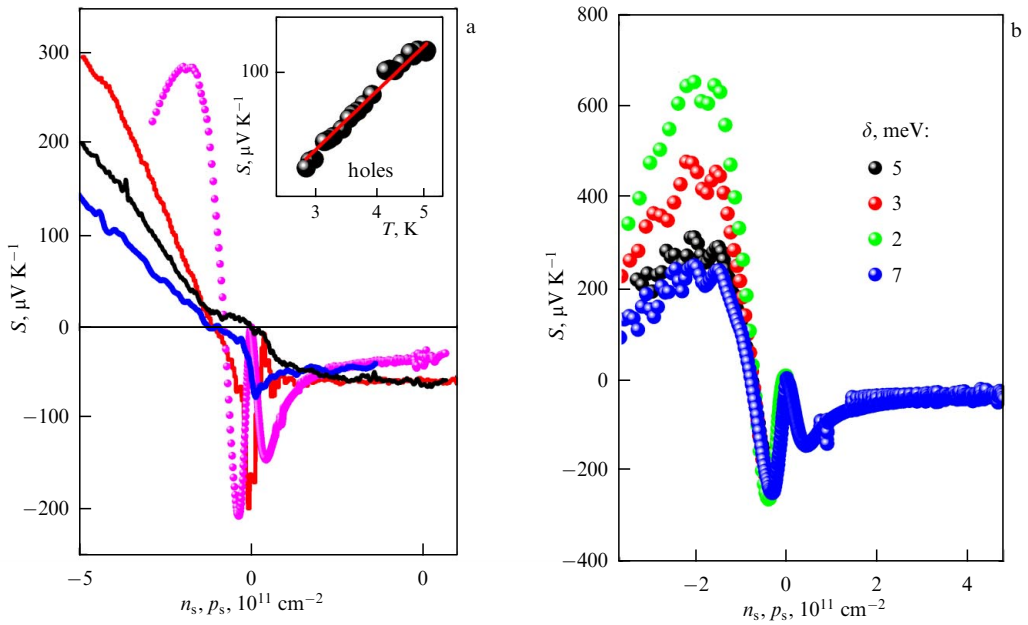

Figure 20. (a) Seebeck coefficient as function of density measured for different samples: Red line — sample A, blue line — sample B, black line — sample C, $T = 4.2$ K. Inset is temperature dependence of Seebeck coefficient for holes ($V_g = 4$ V); solid red line $S \sim T^{1.5}$. Balls — theory calculated from Mott equation with parameters for density of states: $\delta = 5$ meV, $\varsigma = 3$ meV. (b) Seebeck coefficient as function of density calculated from Mott relation for different parameters of density of states, $\varsigma = 3$ meV (22), $T = 4.2$ K.

Figure 20a illustrates the thermopower of three samples plotted against density. The plot shows a bipolar behavior that is similar to semimetals discussed in the previous sections. This is expected, since the gate voltage sweeps from the conduction to the valence band, causing the sign of the Seebeck coefficient to change from negative (electrons) to positive (holes), passing through the Dirac point. The inset shows the temperature dependence at a selected density for the hole side. The thermo signal follows $\sim T^{1.5}$, which is close to the expected behavior for diffusive thermopower. Near the charge neutrality point, one can observe fluctuating behavior that is not reproducible from sample to sample. This behavior is likely due to the strong variation in the density of states near this point and the mobility with energy. One can expect that these fluctuations are sample dependent due to disorder.

Before comparing our experimental results with Mott relations, it is important to note that our system is highly unusual. The hole band is composed of two very different

types of carriers: one is the Dirac particle with a very small effective mass that strongly varies with energy, while the other represents holes with a large effective mass. This unique combination is responsible for different transport peculiarities, which can be harnessed to enhance the thermoelectric performance of our system.

First, the variation in the density of states with energy as the chemical potential approaches the heavy hole band results in an enhancement of the Seebeck coefficient. Second, under these conditions, inter-band and intersubband scattering make an essential contribution to the thermopower. Unfortunately, the presence of disorder can greatly affect all these advantages and smooth out the effects. However, further improvement in the quality of the material holds great promise for its thermoelectric potential.

Figure 20a shows a comparison with the Mott equation. The simple model demonstrates a strong enhancement of the thermopower signal in the valence band, where transport peculiarities are expected in the energy spectrum. Moreover, the theoretical curve exhibits additional features near the CNP, where transport characteristics rapidly vary with energy. Figure 20b shows theoretical curves calculated from the Mott ratio for different broadening parameters (δ). The curves demonstrate that smaller values of δ lead to higher derivatives of the density of states and relaxation time, resulting in an increase in thermopower.

It should be noted that obtaining a more precise description and fit of the experiment requires a more exact knowledge of the density of states in this system. However, as of yet, obtaining such exact knowledge of the density of states in this system has not been possible.

To simplify the model, we did not include inelastic scattering between Dirac and heavy holes, which can significantly modify the thermopower, as demonstrated in 2D semimetals, particularly in the valence band at high temperatures ($T > 5$ K). However, we acknowledge that this is an important aspect that will be studied in future research at high temperatures.

Another important contribution is phonon drag, which dominates at temperatures above 4.2 K, as has been demonstrated in Sections 5 and 6. At lower temperatures, it is comparable to the diffusion contribution. However, it should be noted that the theory for phonon drag in a gapless HgTe quantum well for particles with a Dirac spectrum has not yet been developed, and thus, this problem will be left for future research.

7.3 Conclusion

There are several features that make the 2D Weyl semimetal in a gapless HgTe quantum well an attractive system for thermoelectricity studies. The single Dirac cone responsible for several important consequences can be derived from the Mott relation and can enhance the Seebeck coefficient. In contrast to conventional 2D systems, the density of states varies with energy, and the transport time has a strong energy dependence. The coexistence of Dirac and heavy holes creates an unusual situation for manipulating the band degeneracy. Converging different electronic bands by aligning their band extrema within the energy difference of a few $k_B T$ can also increase the thermoelectric efficiency.

In this study, we have measured the Seebeck coefficient in a 6.3-nm HgTe well and demonstrated that some of these possibilities can be developed in this system. The behavior of the Seebeck coefficient is explained based on the Mott relation. However, it should be noted that such a description is dependent on the model of the density of states, especially broadening due to disorder and inhomogeneities.

8. Concluding remarks

To sum up, this article uses the thermopower of 2D, 3D topological insulators and 2D semimetals hosted in HgTe-based materials as a research platform to discuss the most basic physical issues of the mechanism of scattering in semiconductors and metals. Compared with the past, we have a certain understanding of the conduction mechanism of two-dimensional topological insulators. However, there is a long way to go, and there are still many problems in the study of the scattering mechanism of 2D and 3D topological insulators, but this can also point out the need for further research related to two-dimensional materials. Here are some issues that need to be considered:

(1) The mechanism responsible for the scattering between helical edge states needs to be investigated. Elastic back-scattering is expected to be suppressed due to time reversal symmetry. However, the thermopower due to edge states requires a strong energy-dependent scattering mechanism.

(2) It is crucial to have accurate knowledge of the behavior of the bulk conductivity and density of states in both the bulk band gap and the conduction and valence bands in two-dimensional topological insulators.

(3) In three-dimensional TIs, it is necessary to have accurate knowledge of 2D–3D scattering. In the region where 2D electrons and 3D bulk holes coexist, it is challenging to distinguish the thermopower mechanism due to electron-hole scattering. This scattering can modify the temperature dependence of $S_{xx}(T)$.

(4) Detailed investigations are necessary to understand the transport properties near the CNP in 2D Weyl semimetals in gapless HgTe quantum wells. Percolation along zero energy channels may lead to peculiarities in the thermopower coefficient.

(5) In 2D Weyl semimetals hosted in an HgTe 6.3-nm quantum well, hole–hole scattering in the valence band is much stronger than impurity scattering. This leads to dominant interaction behavior in transport and can significantly modify thermoelectric effects at high temperatures.

Based on current progress and existing challenges, there is still much work that needs to be done in the future. Previous theoretical work has mainly focused on ideal TI structures for thermoelectricity, with little attention given to the complex scattering mechanism between helical or surface states and the bulk.

Moreover, various ways of controlling TI helical and surface states, such as through topological phase transitions (e.g., applying an electric field or strain) or symmetry breaking (e.g., applying a magnetic field to break time reversal symmetry), remain to be explored for designing new thermoelectric devices.

To further enhance the efficiency of thermoelectricity in TI nanostructures and to manifest the advantage of the high mobility of TI helical or surface states due to the strong energy dependence of the scattering mechanism, it is desirable to develop new techniques to introduce disorders and defects into TI materials.

In addition, more systematic measurements, including the influence of electron-electron scattering, are needed in order to amplify the Seebeck effect for thermoelectricity applications.

G.M.G., A.D.L., E.B.O., and Z.D.K. performed the experiment, N.N.M synthesized the crystals, G.M.G. and A.D.L. provided the theoretical framework, and G.M.G. and E.B.O. wrote the manuscript with input from all the authors. G.M.G. and Z.D.K. supervised the work. All the authors have read and agreed to the published version of the manuscript.

Financial support for this work from the Ministry of Science and Higher Education of the Russian Federation, the Sao Paulo Research Foundation (FAPESP) Grant No. 2021/12470-8, and the National Council for Scientific and Technological Development (CNPq) is acknowledged.

The data presented in this study are available on request from the corresponding author.

We thank M.V. Entin, L.I. Magarill, and O.E. Raichev for the helpful discussions.

References

1. Ziman J M *Principles of the Theory of Solids* 2nd ed. (Cambridge: Cambridge Univ. Press, 1972)
2. Shi X-L, Zou J, Chen Z-G *Chem. Rev.* **120** 7399 (2020)
3. Qi X-L, Zhang S-C *Rev. Mod. Phys.* **83** 1057 (2011)
4. Qi X-L, Zhang S-C *Phys. Today* **63** (1) 33 (2010)
5. Hasan M Z, Kane C L *Rev. Mod. Phys.* **82** 3045 (2010)
6. Pankratov O A *Phys. Usp.* **61** 1116 (2018); *Usp. Fiz. Nauk* **188** 1226 (2018)
7. Durnev M V, Tarasenko S A *Ann. Physik* **531** 1800418 (2019)
8. Tarasenko S A *Phys. Usp.* **61** 1026 (2018); *Usp. Fiz. Nauk* **188** 1129 (2018)
9. Vedeneev S I *Phys. Usp.* **60** 385 (2017); *Usp. Fiz. Nauk* **187** 411 (2017)
10. Xu Y, Gan Z, Zhang S-C *Phys. Rev. Lett.* **112** 226801 (2014)
11. Gusev G M et al. *Solid State Commun.* **302** 113701 (2019)
12. Kvon Z D et al. *Phys. Usp.* **63** 629 (2020); *Usp. Fiz. Nauk* **190** 673 (2020)
13. König M et al. *Science* **318** 766 (2007)
14. König M et al. *J. Phys. Soc. Jpn.* **77** 031007 (2008)
15. Roth A et al. *Science* **325** 294 (2009)
16. Kvon Z D et al. *JETP Lett.* **87** 502 (2008); *Pis'ma Zh. Eksp. Teor. Fiz.* **87** 588 (2008)
17. Gusev G M et al. *Phys. Rev. Lett.* **104** 166401 (2010)
18. Büttner B et al. *Nature Phys.* **7** 418 (2011)
19. Kozlov D A et al. *JETP Lett.* **96** 730 (2013); *Pis'ma Zh. Eksp. Teor. Fiz.* **96** 815 (2012)
20. Hasan M Z, Moore J E *Annu. Rev. Condens. Matter Phys.* **2** 55 (2011)
21. Gusev G M et al. *2D Mater.* **9** 015021 (2022)
22. Ivanov Yu V, Burkov A T, Pshenay-Severin D A *Phys. Status Solidi B* **255** 1800020 (2018)
23. Xu N, Xu Y, Zhu J *npj Quantum Mater.* **2** 51 (2017)
24. Ngabonziza P *Nanotechnology* **33** 192001 (2022)
25. Kalantari M H, Zhang X *Nanomaterials* **13** 117 (2023)
26. D'yakonov M I, Khaetskii A V *Sov. Phys. JETP* **55** 917 (1982); *Zh. Eksp. Teor. Fiz.* **82** 1584 (1982)
27. Gerchikov L G, Subashiev A V *Phys. Status Solidi B* **160** 443 (1990)
28. Novik E G et al. *Phys. Rev. B* **72** 035321 (2005)
29. Raichev O E *Phys. Rev. B* **85** 045310 (2012)
30. Gospodaric J et al. *Phys. Rev. B* **104** 115307 (2021)
31. Dantscher K M et al. *Phys. Rev. B* **92** 165314 (2015)
32. Xu Y, Gan Z, Zhang S-C *Phys. Rev. Lett.* **112** 226801 (2014)
33. Hsu C-H et al. *Semicond. Sci. Technol.* **36** 123003 (2021)
34. Schmidt T L et al. *Phys. Rev. Lett.* **108** 156402 (2012)
35. Maciejko J et al. *Phys. Rev. Lett.* **102** 256803 (2009)
36. Kainaris N et al. *Phys. Rev. B* **90** 075118 (2014)
37. Ström A, Johannesson H, Japaridze G I *Phys. Rev. Lett.* **104** 256804 (2010)
38. Crépin F et al. *Phys. Rev. B* **86** 121106 (2012)
39. Budich J C et al. *Phys. Rev. Lett.* **108** 086602 (2012)
40. Hsu C-H et al. *Phys. Rev. B* **96** 081405 (2017)
41. Hsu C-H *Phys. Rev. B* **97** 125432 (2018)
42. Väyrynen J I, Pikulin D I, Alicea J *Phys. Rev. Lett.* **121** 106601 (2018)
43. Väyrynen J I, Goldstein M, Glazman L I *Phys. Rev. Lett.* **110** 216402 (2013)
44. Väyrynen J I et al. *Phys. Rev. B* **90** 115309 (2014)
45. Essert S, Krueckl V, Richter K *Phys. Rev. B* **92** 205306 (2015)
46. Aseev P P, Nagaev K E *Phys. Rev. B* **94** 045425 (2016)
47. Wang J, Meir Y, Gefen Y *Phys. Rev. Lett.* **118** 046801 (2017)
48. Novelli P et al. *Phys. Rev. Lett.* **122** 016601 (2019)
49. Delplace P, Li J, Büttiker M *Phys. Rev. Lett.* **109** 246803 (2012)
50. Kurilovich P D et al. *JETP Lett.* **106** 593 (2017); *Pis'ma Zh. Eksp. Teor. Fiz.* **106** 575 (2017)
51. Sablikov V A, Sukhanov A A *Phys. Rev. B* **103** 155424 (2021)
52. Chou Y-Z, Nandkishore R M, Radzihovsky L *Phys. Rev. B* **98** 054205 (2018)
53. Bindel J R et al. *Nature Phys.* **12** 920 (2016)
54. Gusev G M et al. *Phys. Rev. B* **84** 121302 (2011)
55. Rahim A et al. *2D Mater.* **2** 044015 (2015)
56. Gusev G M et al. *2D Mater.* **6** 014001 (2019)
57. Olshanetsky E B et al. *Phys. Rev. Lett.* **114** 126802 (2015)
58. Gusev G M et al. *Sci. Rep.* **9** 831 (2019)
59. Gusev G M et al. *Phys. Rev. B* **89** 125305 (2014)
60. Parfenov O E, Shklyaruk F A *Semiconductors* **41** 1021 (2007); *Fiz. Tekh. Poluprovodn.* **41** 1041 (2007)
61. Brüne C et al. *Phys. Rev. Lett.* **106** 126803 (2011)
62. Brüne C et al. *Phys. Rev. X* **4** 041045 (2014) DOI:10.1103/PhysRevX.4.041045
63. Kozlov D A et al. *Phys. Rev. Lett.* **112** 196801 (2014)
64. Kozlov D A et al. *Phys. Rev. Lett.* **116** 166802 (2016)
65. Ziegler J et al. *Phys. Rev. Research* **2** 033003 (2020)
66. Müller V L et al. *Nano Lett.* **21** 5195 (2021)
67. Olshanetsky E B et al. *JETP Lett.* **89** 290 (2009); *Pis'ma Zh. Eksp. Teor. Fiz.* **89** 290 (2009)
68. Entin M V et al. *J. Exp. Theor. Phys.* **117** 933 (2013); *Zh. Eksp. Teor. Fiz.* **144** 1068 (2013)
69. Gusev G M et al. *JETP Lett.* **107** 789 (2018); *Pis'ma Zh. Eksp. Teor. Fiz.* **107** 814 (2018)
70. Jost A et al. *Proc. Natl. Acad. Sci. USA* **114** 3381 (2017)
71. Gusev G M et al. *Nanomaterials* **11** 3364 (2021)
72. Hwang E H, Das Sarma S *Phys. Rev. B* **67** 115316 (2003)
73. Nagaev K E, Manoshin A A *Phys. Rev. B* **102** 155411 (2020)
74. Nagaev K E *Phys. Rev. B* **106** 085411 (2022)
75. Pal H K, Yudson V I, Maslov D L *Lithuanian J. Phys.* **52** 142 (2012)
76. Murzin S S et al. *JETP Lett.* **67** 113 (1998); *Pis'ma Zh. Eksp. Teor. Fiz.* **67** 101 (1998)
77. Kravchenko V et al. *Phys. Rev. B* **59** 2376 (1999)
78. Li S, Maslov D L *Phys. Rev. B* **98** 245134 (2018)
79. Lee W-R, Michaeli K, Schwiete G *Phys. Rev. B* **103** 115140 (2021)
80. Takahashi K et al. *Phys. Rev. B* **107** 115158 (2023)
81. Gantmakher V F, Levinson I B *Sov. Phys. JETP* **47** 133 (1978); *Zh. Eksp. Teor. Fiz.* **74** 261 (1978)
82. Zavaritskii N V, Kvon Z D *JETP Lett.* **38** 97 (1983); *Pis'ma Zh. Eksp. Teor. Fiz.* **38** 85 (1983)
83. Entin M V, Magarill L I, to be published
84. Van de Walle C G *Phys. Rev. B* **39** 1871 (1989)
85. Qteish A, Needs R J *Phys. Rev. B* **45** 1317 (1992)
86. Gusev G M et al. *Phys. Rev. B* **96** 045304 (2017)
87. Zuev Yu M, Chang W, Kim P *Phys. Rev. Lett.* **102** 096807 (2009)
88. Mahmoodian M M, Entin M V *Phys. Status Solidi B* **256** 1800652 (2019)
89. Mahmoodian M M, Entin M V *Phys. Rev. B* **101** 125415 (2020)
90. Dobretsova A A et al. *JETP Lett.* **104** 388 (2016); *Pis'ma Zh. Eksp. Teor. Fiz.* **104** 402 (2016)